

Analyzing, quantifying and optimizing crossflow microfiltration of fine
suspensions

Levy Amar

Submitted in partial fulfillment of the
requirements for the degree of
Doctor of Philosophy
in the Graduate School of Arts and Sciences

COLUMBIA UNIVERSITY

2019

© 2019
Levy Amar
All rights reserved

ABSTRACT

Analyzing, quantifying and optimizing crossflow microfiltration of fine suspensions

Levy Amar

Steady state crossflow microfiltration (CMF) is an important and often necessary means for varying sized particle separation. It has been widely used in both industrial and biomedical processes, including a wearable water removal device intended to maintain end stage renal disease (ESRD) patients euvolemic.

For kidney replacement therapies, there are few options available. Kidney transplantation still represents the optimal treatment for ESRD patients, even though it often requires daily post-transplant medication including immunosuppressant drugs to avoid rejection of the transplanted organ. The transplanted kidney itself has an average lifespan of only 10 years. The biggest engineering contribution to the cited problem was made about 60 years ago with the invention of dialysis machines (or some variation thereof). Dialysis still represents the optimal and most widely used therapeutic approach to renal replacement during long waits on a transplant list. The present-day dialysis system is bulky, totally mechanical, and extracorporeal, leading to a widely used therapy that is only effective in extracting water and toxins out of the blood-stream, but still with major drawbacks (*i.e.* intermittent treatments, 5-hours thrice-weekly, and forcing clinic-centered therapy) that are permanently costly. These drawbacks pose a major impediment to rehabilitation or any other lifestyle activity such as working or studying. Of all the vital organs, the kidney is both the most subtle in its homeostatic action and the most complex in terms of the

structures it uses to accomplish its action. This thesis proposes a single facet of the multiple complexity of this vital organ: filtration.

To that effect, CMF of blood suspensions through a microsieve were studied. Experiments, reported here, have correlated macroscopic measurements - filtration rates, transmembrane pressures (TMP), shear rates - during filtration through a photolithographically pored semiconductor membrane with direct observation of erythrocyte behavior at the filtering surface. Erythrocytes, the preponderant particles in blood, are believed to dominate filtration resistance. At low filtration rates (low TMP), erythrocytes roll along the filter, but at higher rates (higher TMP), there is an increasing probability of their sticking to the sieve.

The design of membrane separation processes requires quantitative expressions relating the separation performance to material properties. The factors controlling the performance of CMF have been and continue to be extensively reviewed. There have been a number of influential approaches in CMF. Most have been based on the rate limiting effects of the concentration polarization of rejectate at the sieving surface. Various empirical and intuitive models exist which have been critically assessed in terms of their predictive capability and applicability to CMF from a microfluidic channel. Chapter 1 summarizes this assessment.

Chapter 2 takes a closer look at how erythrocytes behave in a microfiltration environment. Maximum steady-state filtration flux has been observed to be a function of wall shear rate, as predicted by any conventional cross-flow filtration theory, but to show weak dependence on erythrocyte concentration, contrary to theory based on convective diffusion. Flux is known to be directly proportional to the TMP; however, since the pressure drop across a channel decreases along the direction of flow, TMP must modulate along the channel (highest at the leading edge

of the membrane and lowest at the trailing edge). As a consequence, an area of stuck particles growing from the inlet (regimen of high TMP) has been observed, leading to a “fouling cascade.” Post-filtration scanning electron micrographs revealed significant capture and deformation of erythrocytes in all filter pores in the range 0.25 to 2 μm diameter. This was then found to form a self-assembled partially complete monolayer. Filtration rates through these filters were reported and a largely unrecognized mechanism was proposed, which allows for stable filtration in the presence of substantial cell layering.

Chapter 3 proposes a microfiltration model that pertains to non-deformable particles that are large enough to intrude significantly into the shear layer of a microchannel. A stable, stationary multilayer of particles was studied, whose thickness is shear-limited. The structure and parameters in that limit of steady filtration in this environment was then identified. A steady cake-layer thickness was observed and because of the simple geometry afforded by uniform spheres, the force balance, cake resistance, and filtration rate were derived from first principles. The good fit of the data to the proposed mechanism, provides a firm basis for the semi-quantitative analysis of the behavior of more complex suspensions.

Finally, in Chapter 4, a design methodology was imposed to maintain the TMP constant throughout the whole sieving surface by introducing a flow chamber beneath and parallel to the sieve’s main flow. Co-current filtration was found to allow the TMP to remain stable along the membrane surface, enabling the entire sieve to perform optimally, and thus allowing greater stable filtration rates to be achieved. Co-current flow conditions allowed for twice as much filtration flux compared to a conventional CMF modality.

Table of Contents

List of Figures, Tables, and Illustrations.....	ii
Chapter 1 – Introduction.....	1
Chapter 2 – Erythrocyte Fouling on Micro-engineered Membrane.....	14
Chapter 3 – Modeling of Fouling in Cross-flow Microfiltration of Suspensions.....	45
Chapter 4 – Co-current Crossflow Microfiltration in a Microchannel.....	75
Chapter 5 – Conclusion.....	96

List of Figures, Tables, and Illustrations

Figure 2-1: a) Macroscopic image of Microsieve. b) Scanning electron micrographs of microsieves with diverse pore sizes and geometries (top view), pore size depicted under each corresponding micrograph. c) Cross-sectional schematic of microsieve beneath a weep hole with the thin perforated Si_3N_4 ($<1 \mu\text{m}$) layer over the $500 \mu\text{m}$ thick silicon support.....19

Figure 2-2: a) Layout of the microfluidic device. b) Semi-assembled device. c) Crossflow schematics - blood channel layer. Channel dimensions: Length (L) = 3 cm, Width (W)= 9 mm, Height (H)= $200 \mu\text{m}$. (The actual channel height was confirmed by water pressure-flow measurements – see text, Section 2.6).....21

Figure 2-3: System arrangement including location of the pressure sensors: Blood in (P_2), Blood out (P_1), and Plasma out (P_3).....22

Figure 2-4: a) Scanning electron micrograph of a single erythrocyte on a $0.45 \mu\text{m}$ microsieve retaining its biconcave shape once filtration was stopped. b) 3D enhancement with WXsM software⁵⁸ of an atomic force micrograph of a single erythrocyte, fixed with 2% glutaraldehyde, on a $0.8 \mu\text{m}$ microsieve entrapped because of filtration (high TMP).....26

Figure 2-5: Scanning electron micrograph of Si_3N_4 Microsieve with $300 \mu\text{m}$ round Membrane Fields (with $0.25 \mu\text{m}$ pores) packed with “deformed” erythrocytes solely at pored regions, indicating that erythrocytes are not chemically bound to Si_3N_4 , but mechanically anchored within the pores. Measurement were made at maximum flux and high shear rate ($0.35 \text{cm}/\text{min}$ at 8000s^{-1}). Images acquired after chasing the system with 2% glutaraldehyde solution at maximum filtrate rate. Thus, the cellular behavior shown should closely approximate that during stable filtration. Magnification: 120X (L), 400X (M), 1900X (R).....27

Figure 2-6: Scanning electron micrograph of a deformed erythrocyte that was drawn into the pores (0.25 μ m pores) during filtration and released once filtration was stopped. a) Fragment scanned at 14000X. b) Top view of the pillars. 3D enhancement with WXsM software.⁵⁸ c) 3D enhancement of b, 55 $^{\circ}$ view.....28

Figure 2-7: Experimental measurement of total resistance due to filtration and erythrocyte accumulation at the sieve surface. Filtration rate is directly proportional to shear rate. As can be seen, the maximum filtration rate at steady state is nearly the same irrespective of the pore geometry and the fraction of sieve open area.....30

Figure 2-8: The effect of hematocrit on sieve performance is not present. Contrary to classical theory, higher solute concentration was not observed to have an effect on filtration rate.....31

Table 2-1: Intrinsic resistance (R_M) of each membrane.....37

Figure 2-9: Maximum filtration rate is linearly dependent on shear rate (2000 - 8000 s^{-1}), however, independent of solute concentration (hematocrit) at each shear rate.....38

Table 2-2: Calculated fluxes ($J = Q_f/A_m$) for each pore geometry. Q_f represents maximum filtration rate at its corresponding shear rate, and A_m corresponds to the sieving area of 2.2 cm^238

Figure 2-10: Transmembrane pressure profile: Initial rising slope represents the time to reach steady state (section A). Plateau represents stable filtration under subcritical TMP (section B). Steep rising represents unstable filtration with cellular accumulation and jamming of the filtering membrane when filtrate rate was increased above critical TMP (section C). TMP drops back to 0 torr when filtrate pump is stopped (at 560s).....39

Figure 3-1: Forces affecting buildup of particles, where F_h is the shear force exerted by the main flow and F_v is the drag force of the filtrate flow.....50

Figure 3-2: Transformation to spherical coordinates, where51

Figure 3-3: Layout of the microfluidic device, top and side views.....54

Figure 3-4: Sample transmembrane pressure (TMP) profile, given a filtration flowrate of 0.020 mL/min, for various main flowrates (Q_m).....61

Table 3-1: $Q_{m,min}$ at different filtration rates (Q_f) for two different particle sizes.....61

Figure 3-5: Packed bed thickness as a function of Q_m and Q_f using 7.9 μm bead suspension. Packed bed thickness decreases as a function of Q_m and increases as a function of Q_f . For each data set, the Blake-Kozeny calculation of packed bed porosity is applied to test the experimental data. Since the packed bed is incompressible, assuming the porosity to be independent of the imposed differential pressure.⁴² The porosity intrinsic to the sphere geometry, ϵ , is reported to be as 0.35-0.45.³⁵.....63

Table 3-2: Calculated porosity using the Blake-Kozeny equation for $Q_f = 0.030$ mL/min at varying Q_m64

Table 3-3: Calculated wall shear stress of filtrations at constant $Q_f = 0.030$ mL/min for varying Q_m65

Table 3-4: Average critical shear stress (τ_c) at different filtration rates (Q_f) for two different sizes of particles used. The critical shear stress increased with filtration rate. Smaller bead results in higher critical shear stress.....65

Figure 3-6: Critical shear stress versus filtrate flowrate for various bead diameters. Critical shear stress at each filtration rate (Q_f) was plotted to demonstrate a monotonically increasing trend, aligned with our theoretical prediction.....66

Figure 4.1. Pressure profiles of conventional (column A), and co-current (column B) filtration configurations. The first row (red) of the figure shows the expected pressure drop down the feed (blood) channel. The second row (yellow) shows, left, the usual, constant pressure in the filtrate (plasma) channel, and, right, a filtrate collecting channel with plasma flow configured to establish in the channel a pressure gradient that parallels that in the feed channel. The third row (green) shows, left, how a computed transmembrane pressure (TMP) drops across the channel length to the point it can produce backflow in the presence of an invariant filtrate pressure. And (right) how a varying plasma channel pressure can produce a constant transmembrane pressure. The straight-line variation in blood pressure in all panels of the figure presumes a low ratio of filtration flow to channel flow.....77

Figure 4-2. a) Layout of the microfluidic device. b) Semi-assembled device. c) Crossflow schematic – blood/plasma channel layer. Channel dimensions: Length (L) = 3 cm, Width (W)= 9 mm, Blood Height (2B)= 200 μ m, Plasma Height (2B)= 100 μ m. The actual channel height was confirmed by water pressure-flow measurements – see Appendix.....80

Figure 4-3. System arrangement including location of the pressure sensors: Blood in (P_1), Blood out (P_2), Plasma in (P_3), and Plasma out (P_4).....82

Table 4-1. Calculated fluxes ($J = Q_f/A_m$) for each sieving configuration. Q_f represents maximum filtration rate at its corresponding shear rate, and A_m corresponds to the sieving area of 2 cm^285

Figure 4-4. Compares filtration with cTMP (blue squares) to filtration without cTMP (red triangles). The average ratio of the filtrate fluxes through a sieving area of 2 cm² over each set of points is 1.9 ± 0.0586

Table 4-2. Calculated fluxes ($J = Q_f/A_m$) for each sieving configuration, with Q_f representing the maximum filtration rate at its corresponding shear rate, and A_m corresponding to the sieving area of 4 cm².....87

Figure 4-5. Compares filtration with cTMP (blue squares) to filtration without cTMP (red triangles). In theory (green diamonds), the cTMP advantage should be exactly twofold, given that the filtration rate is insignificant relative to the plasma flow. However, fluxes under variable TMP configuration significantly diminish when a longer flow path (4 cm²) was studied. Most probably due to cumulative accumulation membrane fouling from multiple runs.....88

Acknowledgement

There are many people that have earned my gratitude for their contribution to my time in graduate school. More specifically, I would like to thank the following group of people, without whom this thesis would not have been possible: my thesis mentor, thesis committee members, my lab partners, funding agencies, and my family and friends.

My Advisor

First, I am indebted to my thesis mentor, Dr. Edward F. Leonard for offering me the opportunity to join the Artificial Organs Research Laboratory. Since my first day in graduate school, Dr. Leonard believed in me and gave me endless support. On the academic level, Dr. Leonard taught me critical thinking, and the fundamentals of conducting scientific research. Under his supervision, I learned how to define a research problem, find a solution to it, and finally publish the results. On a personal level, Ed inspired me by his hardworking and passionate attitude. To summarize, I would give Professor Leonard most of the credit for me becoming the kind of scientist and person I am today.

A special thanks to Mrs. Sheri Leonard for her continued encouragement and for being so supportive during all the times I borrowed her husband away.

Thesis Committee Members

Besides my advisor, I would like to thank the rest of my dissertation committee members: Dr. Gordana Vunjak-Novakovic, Dr. Henry Hess, Dr. Andrew Laine, and Dr. James Hone for their invaluable support and advice.

My Lab partners

I would like to thank my lab partners for their continued support. This dissertation would not have been possible without the intellectual contribution of Professor Michael Hill and Dr. Robert von Gutfeld. Moreover, I am thankful to Dr. Cees J. M. van Rijn, Dr. Nopphon Weeranoppanant, Dr. Monica Faria, Dr. Daniela Guisado, and Evelyn Tong for their collaboration and contribution in various projects related to this dissertation. I would also like to thank our whole medical team, the Columbia Medical Center Blood Bank and blood donors, especially Dr. Stanley Cortell, Dr. Joseph Schwartz, Ms. Carin Campbell and most especially the late Dr. James Jones.

Funding Agencies

Support for this work was provided in part by Grant 1R21HL088162 from the National Institute of Health, and Vizio Medical Devices, LLC.

My Family and Friends

Last, but not least, I would like to express my deepest gratitude to my family and friends. This dissertation would not have been possible without their warm love, continued patience, and endless support.

Chapter 1

Introduction

This thesis is primarily focused on the contemporary medical problem of removing plasma from blood with appropriate concern for therapeutic and physical constraints. An attractive approach, that is taken here is microfiltration. Practical microfiltration was first attempted at the beginning of the 20th century using new recipes for synthetic microporous membranes based on cellulose. In 1907, Bechhold¹ discovered, while filtering colloidal suspensions, that a flow parallel to such a filter medium increased the amount of filtrate before the filter medium was blocked by formation of a compact layer. His work was the first recognition of sheared filtration, an essential element of crossflow microfiltration (CMF).

In CMF, the fluid to be filtered flows parallel to the membrane surface and permeates through the membrane due to a pressure difference. The fluid dynamics of CMF reduce membrane fouling by allowing removal of what is to be held back, the retentate, at a rate commensurate with what is to be filtered, the permeate, (*i.e.* balancing retentate removal against a steady filtration rates).² However permeate flow typically declines due to membrane clogging.³ According to the frequently referenced Michaels' model,⁴ an increase in applied pressure to overcome clogging produces a temporary increase in flux, but brings more solute to the filtering surface, increasing the hydraulic resistance to solvent flow, thereby reducing the flux to its original level. A more rapid flow of feed solution across the membrane is beneficial, acting 'sweep' the surface, reducing retentate accumulation.³⁻⁷ Shear also inhibits adhesion of foulants other than the principal retentate that can plug pores at the membrane surface.⁷ Multiple analyses of this situation are available and are summarized in the chapters of this thesis, but most of them deal with macroscopic flow channels, while the goal of this work is to understand CMF in microfluidic flows.

1.1 Crossflow Microfiltration in Blood Processing

Today, CMF is a standard operational mode in many medical membrane applications.⁸⁻¹⁰ These include blood plasma fractionation and purification,¹¹⁻¹⁵ cellular analysis and separation,¹⁶⁻²¹ circulating tumor cells isolation,²² concentration cell culture perfusion,²³⁻²⁵ washing of bacterial cells,^{15,26-30} Separation of plasma from flowing blood is a component of several therapies currently under development.³¹⁻³³ High-flux plasma filtration in a microfluidic environment could permit ambulatory separation of plasma from blood with a small wearable device. The recent availability of photolithographically defined pore fields^{34,35} offers a well-defined barrier with a low intrinsic membrane resistance that appears capable of separating plasma from erythrocytes.³⁶ Filtration through these pore fields of plasma from blood and of model polymer spheres is addressed in this thesis, in particular as an adjunct to clinical hemodialysis where simultaneous filtration and dialysis has proven troublesome.

1.2 The Problem with Current Dialysis and the Clinical Relevance of an Extracorporeal Device

Hemodialysis is one of three renal replacement therapies (the other two being peritoneal dialysis and kidney transplant) for end stage renal disease (ESRD) patients.³⁷ Hemodialysis achieves the extracorporeal removal of waste products (solutes) such as urea, creatinine, and many other substances from the blood when the kidneys have failed. Water, the solvent for these substances, cannot be removed by dialysis and must be removed by imposing a pressure gradient across the dialysis membrane, that is by CMF. A substantial literature has arisen to suggest that simultaneous dialysis of solutes by dialysis and solvent (water) are physiologically inconsistent.³⁸

The author's laboratory has proposed a wearable system for removing water outside the time spent in dialysis. It consists of a two-step continuous process conducted whenever dialysis is not being conducted, *e.g.* a wearable water-removal system, in which plasma is first obtained from blood by CMF, then ultrafiltered to extract water (plus small molecules), and then returned to the bloodstream. The wearable slow, continuous, extracorporeal filter would assist mainly in extra water removal to maintain patients hemodynamically stable (euvoemia).

1.3 Crossflow Filtration Theory

The design of membrane separation processes, like all other processes, requires quantitative expressions relating separation performance to material properties. The factors controlling the performance of crossflow microfiltration are extensively reviewed.^{7,39-42} There have been a number of interesting approaches in this field.^{7,43,44} Most have been based on the rate limiting effects of concentration polarization of colloids at the membrane surface.³ Various rigorous, empirical and intuitive models exist, which have been critically assessed in terms of their predictive capability and applicability.³⁻⁷ However, these (macrofluidic) models fail to address some critical factors associated with CMF of cells and particles from a microfluidic channel. This is what motivated the work in Chapters 2 and 3 of this thesis.

1.4 The Problem of Macrofiltration in Microdevices

The fundamental problem in any continuous crossflow filtration system is keeping the filter clear of the retentate, which is left behind, as the filtrate passes through. If, as usual, the feed passes in shear flow over the filter, it must carry the retentate toward and through an exit port. Because the transverse feed velocity at the filter surface is zero, the components of the retentate must be both moved away from the filter surface and then be carried to an exit.^{39,40} All filtration theories seek

to describe how this occurs. If the retentate particles are small molecules, back diffusion into the feed stream may suffice.^{3,5-7} If the retentate particles are larger, Brownian diffusion of retentate away from the surface will not be fast enough to sustain a reasonable filtration rate. Various authors have postulated other mechanisms for removing retentate.^{41,42,44-47} One postulates random interactions of particles with each other and the flowing stream causing a pseudo-Brownian movement away from the filter surface.⁴⁸ Others have postulated that a moving sludge slides over the filter toward the feed exit.^{7,43} All of these analyses presume that the retentate will not induce fouling of the filter surface or its pores. When fouling occurs, temporal distinctions are in order. The foulant may quickly passivate the filter surface with possible changes in its filtration capacity, after which the system achieves a steady state performance level. Alternatively, fouling may proceed slowly but steadily with the effect of limiting filter performance time. In the worst case, fouling simply shuts the system down.

Microfiltration has different meanings, depending on the experimental conditions.

Microfiltration becomes palpably "micro" when the retentate particles have characteristic dimensions comparable to that of the flow channel. In this circumstance, the discrete nature of the particles must be taken into account, and one may expect specific particle interactions with the filter during shear flow. With particles as large as erythrocytes in a channel not much larger than such particles, molecular diffusion is relatively unimportant and the mechanical interactions among particle layers become dominant.⁴⁹ For steady state to occur, particles cannot accumulate at any given point. Thus, the forces which cause particles to enter a given voxel must be compensated by the forces that allow them to exit. This has been the subject of considerable investigations.^{7,41-43,47} Considering all the details, the net effect must be that each voxel is kept in the steady state by a combination of net axial movement and the tendency for the particles to

move outward due to particle interactions that overcome the forces that brought them to the membrane.^{39,40}

While the above cited studies have provided important contributions to particle motion in crossflow filtration (mostly macrofiltration), they do not translate well to filtration of soft particles in microfluidic systems, particularly under conditions that allow separation of plasma from whole blood. In this thesis, we have described a largely unrecognized mechanism that allows steady state filtration in the presence of substantial cell layering.

1.5 Contribution of this Thesis

The standard approach has been to use pressure during dialysis to superimpose ultrafiltration on top of true dialysis concentration difference. Fluid removal (ultrafiltration) is achieved by altering the hydrostatic pressure of the dialysate compartment, causing free water and some dissolved solutes to move across the membrane along a created pressure gradient.

Unfortunately, there can be undesirable interactions by using pressure to remove a large volume of water during the course of dialysis.³⁸ There exists a physiological reflex, whereby a rapid reduction in blood volume (blood pressure), increases total peripheral resistance, shutting down perfusion of the muscles which contain large amounts of toxins. Therefore, if ultrafiltration is accomplished quickly only during dialysis, it will impede dialysis by effectively hiding the toxins in the muscles.

Thus, there are strong incentives to maintain the expensive, sophisticated, and well supervised (by nephrologists) dialysis system, but relieving the encumbering requirement to remove the large volume of water.⁵⁰ The total effort in which the author's laboratory was engaged, addressed this important issue. The issue is not simple; it involves a way of effectively implementing a

better solution between dialysis to remove fluid overload – which suggests a small portable filtration device. The work of this thesis was directed to solving a large number of problems associated with this motif.

This thesis contributes knowledge which would enable water to be ultrafiltered, not dialyzed, steadily between treatment to present the physician in the clinic with a more euvoletic patient, but still very challenging dialysis. After there were great hope in the laboratory for the use of a two-stage procedure, perfecting this water removal involved a filter which would allow the production of a cell free (plasma) fraction from whole blood. This plasma filtrate could then be heavily ultrafiltered through a classical microporous membrane with far less clotting concerns.

The work in this thesis is directed toward understanding the first-step separation process, identifying the different issues that are involved in making that kind of filtrate. Consequently, there were fundamental issues and mechanistic issues that arose as the project evolved, which were addressed in this thesis. We have analyzed and considered the combined effects of crossflow microfiltration of deformable (chapter 2) and non-deformable (chapter 3) suspensions in a microchannel through a thin, low intrinsic resistance, uniformly pored microsieve. We have also identified a new approach to how, in general, one would filter plasma from blood using microporous membranes. We found the difficulties that may be involved and the methodology which regulates the filtration (chapter 4) to allow stable steady state filtration to be achieved.

In Chapter 2, we study the microfiltration of flowing blood in a microchannel through a semiconductor microsieve.³⁴ Experiments were undertaken with the further aim of obtaining a clearer understanding of deformable particle behavior during filtration so as to enable one to predict plasma extraction from whole blood for a given set of fluidic and filter parameters. We report

filtration rates through these filters and describe a largely unrecognized mechanism that allows stable filtration in the presence of substantial cell layering.

In Chapter 3, we present a new model based on shear-resistant particle immobilization on the filter surface. Microfluidic cross-flow filtration experiments demonstrate a non-negligible bed of particles building up on a filter surface.^{51,52} The layer affects not only the filtrate flux, but also the through flow of retentate.^{53,54} The buildup of particles is rapid, and does not depend upon fouling reactions with the filter surface.^{55,56} The model predicts filtration rates when the mechanical interactions among particles, the suspending fluid, and the filtering surface jointly control layer thickness and thus filtration. This model is shown to be in good agreement with experimental data obtained from isometric polymer beads chosen for ease of analysis.

And finally, in chapter 4, we introduced a carefully designed flow channel on the permeate side beneath the membrane which permits the pressure on the permeate side of the membrane to decrease along the length of the membrane, and thereby lead to a constant TMP (cTMP) along the membrane. This modality allows for the entire membrane to be used at a pressure below that leading to erythrocyte fouling (critical flux),⁵⁷ allowing up to twice as much filtration over that of the naïve configuration employed in Chapter 2.

References

1. Bechhold H. Kolloidstudien mit der Filtrationsmethode. *Zeitschrift für Elektrochemie und angewandte physikalische Chemie* 1907;13:527-33.
2. Knops FNM, Futselaar H, Rácz IG. The transversal flow microfiltration module. Theory, design, realization and experiments. *Journal of Membrane Science* 1992;73:153-61.
3. Mackley MR, Sherman NE. Cross-flow cake filtration mechanisms and kinetics. *Chemical Engineering Science* 1992;47:3067-84.
4. Michaels AS. New separation technique for CPI. *Chemical Engineering Progress* 1968;64:31-&.
5. Zydney AL, Colton CK. A Concentration Polarization Model For The Filtrate Flux In Cross-Flow Microfiltration Of Particulate Suspensions. *Chemical Engineering Communications* 1986;47:1-21.
6. Kromkamp J, Bastiaanse A, Swarts J, Brans G, van der Sman RGM, Boom RM. A Suspension Flow Model For Hydrodynamics And Concentration Polarisation In Crossflow Microfiltration. *Journal of Membrane Science* 2005;253:67-79.
7. Leonard EF, Vassilieff CS. The Deposition Of Rejected Matter In Membrane Separation Processes. *Chemical Engineering Communications* 1984;30:209-17.
8. Jensen KF. Microreaction engineering—is small better? *Chemical Engineering Science* 2001;56:293-303.
9. Ripperger S, Altmann J. Crossflow microfiltration—state of the art. *Separation and Purification Technology* 2002;26:19-31.
10. Yamazoe H, Okuyama T, Suzuki H, Fukuda J. Fabrication of patterned cell co-cultures on albumin-based substrate: applications for microfluidic devices. *Acta biomaterialia* 2010;6:526-33.
11. VanDelinder V, Groisman A. Separation of plasma from whole human blood in a continuous cross-flow in a molded microfluidic device. *Analytical chemistry* 2006;78:3765-71.
12. VanDelinder V, Groisman A. Perfusion in microfluidic cross-flow: separation of white blood cells from whole blood and exchange of medium in a continuous flow. *Analytical Chemistry* 2007;79:2023-30.
13. Burnouf T. Modern plasma fractionation. *Transfusion medicine reviews* 2007;21:101-17.
14. Madrigal JL, Sharma SN, Campbell KT, Stilhano RS, Gijssbers R, Silva EA. Microgels produced using microfluidic on-chip polymer blending for controlled released of VEGF encoding lentivectors. *Acta biomaterialia* 2018.

15. Silva R, Dow P, Dubay R, et al. Rapid prototyping and parametric optimization of plastic acoustofluidic devices for blood–bacteria separation. *Biomedical microdevices* 2017;19:70.
16. Carrère H, Blaszkow F, de Balmann HR. Modelling the clarification of lactic acid fermentation broths by cross-flow microfiltration. *Journal of Membrane Science* 2001;186:219-30.
17. Yeo DC, Wiraja C, Zhou Y, Tay HM, Xu C, Hou HW. Interference-free micro/nanoparticle cell engineering by use of high-throughput microfluidic separation. *ACS applied materials & interfaces* 2015;7:20855-64.
18. Sibbitts J, Sellens KA, Jia S, Klasner SA, Culbertson CT. Cellular Analysis Using Microfluidics. *Analytical chemistry* 2017;90:65-85.
19. Tolan NV, Genes LI, Subasinghe W, Raththagala M, Spence DM. Personalized metabolic assessment of erythrocytes using microfluidic delivery to an array of luminescent wells. *Analytical chemistry* 2009;81:3102-8.
20. Hu S-W, Xu B-Y, Ye W-k, Xia X-H, Chen H-Y, Xu J-J. Versatile microfluidic droplets array for bioanalysis. *ACS applied materials & interfaces* 2015;7:935-40.
21. Barata D, van Blitterswijk C, Habibovic P. High-throughput screening approaches and combinatorial development of biomaterials using microfluidics. *Acta biomaterialia* 2016;34:1-20.
22. Chen H, Cao B, Chen H, Lin Y-S, Zhang J. Combination of antibody-coated, physical-based microfluidic chip with wave-shaped arrays for isolating circulating tumor cells. *Biomedical microdevices* 2017;19:66.
23. Charcosset C. Membrane processes in biotechnology: an overview. *Biotechnology advances* 2006;24:482-92.
24. Mercier M, Maranges C, Fonade C, Lafforgue-Delorme C. Yeast suspension filtration: flux enhancement using an upward gas/liquid slug flow—application to continuous alcoholic fermentation with cell recycle. *Biotechnology and bioengineering* 1998;58:47-57.
25. Rho J, Chung J, Im H, et al. Magnetic nanosensor for detection and profiling of erythrocyte-derived microvesicles. *ACS nano* 2013;7:11227-33.
26. Rossignol N, Vandanjon L, Jaouen P, Quemeneur F. Membrane technology for the continuous separation microalgae/culture medium: compared performances of cross-flow microfiltration and ultrafiltration. *Aquacultural Engineering* 1999;20:191-208.
27. Hodgson P, Leslie G, Fane A, Schneider R, Fell C, Marshall K. Cake resistance and solute rejection in bacterial microfiltration: the role of the extracellular matrix. *Journal of Membrane science* 1993;79:35-53.

28. Frenander U, Jönsson AS. Cell harvesting by cross-flow microfiltration using a shear-enhanced module. *Biotechnology and bioengineering* 1996;52:397-403.
29. Li H, Fane A, Coster H, Vigneswaran S. Observation of deposition and removal behaviour of submicron bacteria on the membrane surface during crossflow microfiltration. *Journal of Membrane Science* 2003;217:29-41.
30. Garcia-Hartjes J, Bernardi S, Weijers CA, et al. Picomolar inhibition of cholera toxin by a pentavalent ganglioside GM1os-calix [5] arene. *Organic & biomolecular chemistry* 2013;11:4340-9.
31. Sollier E, Cubizolles M, Fouillet Y, Achard J-L. Fast and continuous plasma extraction from whole human blood based on expanding cell-free layer devices. *Biomedical microdevices* 2010;12:485-97.
32. Wu W-T, Martin AB, Gandini A, Aubry N, Massoudi M, Antaki JF. Design of microfluidic channels for magnetic separation of malaria-infected red blood cells. *Microfluidics and nanofluidics* 2016;20:41.
33. Martin AB, Wu W-T, Kameneva MV, Antaki JF. Development of a High-Throughput Magnetic Separation Device for Malaria-Infected Erythrocytes. *Annals of biomedical engineering* 2017;45:2888-98.
34. van Rijn CJ, Nijdam W, Kuiper S, Veldhuis GJ, van Wolferen H, Elwenspoek M. Microsieves made with laser interference lithography for micro-filtration applications. *Journal of Micromechanics and Microengineering* 1999;9:170.
35. Ji HM, Samper V, Chen Y, Heng CK, Lim TM, Yobas L. Silicon-based microfilters for whole blood cell separation. *Biomedical microdevices* 2008;10:251-7.
36. Dickson MN, Amar L, Hill M, Schwartz J, Leonard EF. A scalable, micropore, platelet rich plasma separation device. *Biomedical microdevices* 2012;14:1095-102.
37. Pastan S, Bailey J. Dialysis therapy. *New England Journal of Medicine* 1998;338:1428-37.
38. Schneditz D, Zaluska W, Morris A, Fan Z, Kaufman A, Levin N. Effect of ultrafiltration (UF) on peripheral urea sequestration in hemodialysis (HD) patients. *JOURNAL OF THE AMERICAN SOCIETY OF NEPHROLOGY*; 1996: AMER SOC NEPHROLOGY 1725 I ST, NW STE 510, WASHINGTON, DC 20006 USA. p. A1380-A.
39. Blatt WF, Dravid A, Michaels AS, Nelsen L. Solute polarization and cake formation in membrane ultrafiltration: causes, consequences, and control techniques. *Membrane science and technology*: Springer; 1970:47-97.
40. Porter MC. Concentration polarization with membrane ultrafiltration. *Industrial & Engineering Chemistry Product Research and Development* 1972;11:234-48.

41. Vasseur P, Cox R. The lateral migration of a spherical particle in two-dimensional shear flows. *Journal of Fluid Mechanics* 1976;78:385-413.
42. Drew DA, Schonberg JA, Belfort G. Lateral inertial migration of a small sphere in fast laminar flow through a membrane duct. *Chemical engineering science* 1991;46:3219-24.
43. Vassilieff CS. Convective Model Of Cross-Flow Microfiltration. *Advances in Colloid and Interface Science* 1992;40:1-36.
44. Davis RH. Modeling of fouling of crossflow microfiltration membranes. *Separation and purification methods* 1992;21:75-126.
45. Sethi S, Wiesner MR. Modeling of transient permeate flux in cross-flow membrane filtration incorporating multiple particle transport mechanisms. *Journal of membrane science* 1997;136:191-205.
46. Romero CA, Davis RH. Transient model of crossflow microfiltration. *Chemical engineering science* 1990;45:13-25.
47. Segre G, Silberberg A. Behaviour of macroscopic rigid spheres in Poiseuille flow Part 1. Determination of local concentration by statistical analysis of particle passages through crossed light beams. *Journal of Fluid Mechanics* 1962;14:115-35.
48. Zydney A, Colton C. Continuous flow membrane plasmapheresis: theoretical models for flux and hemolysis prediction. *ASAIO Journal* 1982;28:408&hyphen.
49. Kim M-m, Zydney AL. Particle–particle interactions during normal flow filtration: Model simulations. *Chemical Engineering Science* 2005;60:4073-82.
50. Tennankore KK, Chan CT, Curran SP. Intensive home haemodialysis: benefits and barriers. *Nature Reviews Nephrology* 2012;8:515.
51. Tarabara VV, Hovinga RM, Wiesner MR. Constant transmembrane pressure vs. constant permeate flux: effect of particle size on crossflow membrane filtration. *Environmental engineering science* 2002;19:343-55.
52. Smith WO, Foote PD, Busang PF. Packing of homogeneous spheres. *Physical Review* 1929;34:1271-4.
53. Di H, Martin GJ, Sun Q, Xie D, Dunstan DE. Detailed, real-time characterization of particle deposition during crossflow filtration as influenced by solution properties. *Journal of Membrane Science* 2018;555:115-24.
54. Aimar P, Howell J, Turner M. Effects of concentration boundary layer development on the flux limitations in ultrafiltration. *Chemical Engineering Research and Design* 1989;67:255-61.

55. Song L. Flux decline in crossflow microfiltration and ultrafiltration: mechanisms and modeling of membrane fouling. *Journal of Membrane Science* 1998;139:183-200.
56. Di H, Martin GJ, Dunstan DE. A microfluidic system for studying particle deposition during ultrafiltration. *Journal of Membrane Science* 2017;532:68-75.
57. Field RW, Wu D, Howell JA, Gupta BB. Critical flux concept for microfiltration fouling. *Journal of membrane science* 1995;100:259-72.

Chapter 2

Erythrocyte Fouling on Micro-engineered Membranes

(Published: Biomedical Microdevices Journal 2018;20:55)

Levy I. Amar,^{1*} Daniela Guisado,² Monica Faria,² James P. Jones,³ Cees J. M. van Rijn,⁴

Michael I. Hill,² Edward F. Leonard,^{1,2*}

Department of Biomedical Engineering¹, and Chemical Engineering², Columbia University, New York, NY – 10027

Department of Nephrology³, Mount Sinai St. Luke's Roosevelt Hospital, New York, NY – 10025 (deceased)

MicroFluidics and NanoTechnology/ORC⁴, Wageningen University Stippeneng, Wageningen – 6708 WE, The Netherlands

*Corresponding Author: Lia2103@columbia.edu, Leonard@columbia.edu – 500 West 120th street #811, New York, NY - 10027

Topical area: Microfluidics, Separations: Materials, Devices, and Processes, Artificial Organs.

Key words: cross-flow, microfluidics, microfiltration model, microsieve, sieve, photolithography, nanopores, erythrocytes, blood, fouling.

0. Abstract

Crossflow microfiltration of plasma from blood through microsieves in a microchannel is potentially useful in many biomedical applications, including clinically as a wearable water removal device under development by the authors. We report experiments that correlate filtration rates, transmembrane pressures (TMP) and shear rates during filtration through a microscopically high channel bounded by a low intrinsic resistance photolithographically-produced porous semiconductor membrane. These experiments allowed observation of erythrocyte behavior at the filtering surface and showed how their unique deformability properties dominated filtration resistance. At low filtration rates (corresponding to low TMP), they rolled along the filter surface, but at higher filtration rates (corresponding to higher TMP), they anchored themselves to the filter membrane, forming a self-assembled, incomplete monolayer. The incompleteness of the layer was an essential feature of the monolayer's ability to support sustainable filtration. Maximum steady-state filtration flux was a function of wall shear rate, as predicted by conventional crossflow filtration theory, but, contrary to theories based on convective diffusion, showed weak dependence of filtration on erythrocyte concentration. Post-filtration scanning electron micrographs revealed significant capture and deformation of erythrocytes in all filter pores in the range 0.25 to 2 μm diameter. We report filtration rates through these filters and describe a largely unrecognized mechanism that allows stable filtration in the presence of substantial cell layers.

1. Introduction

Crossflow microfiltration is a standard operational mode in many medical and technical membrane applications.¹⁻³ These include blood plasma fractionation and purification,⁴⁻⁸ cellular analysis and separation,⁹⁻¹⁴ circulating tumor cells isolation,¹⁵ concentration cell culture perfusion,¹⁶⁻¹⁸ washing of bacterial cells,^{8,19-23} as well as waste water and buffer purification.^{24,25} Continuous separation of plasma from flowing blood can be accomplished by microfiltration,²⁶⁻²⁸ which is of special interest to the authors.^{16,19,29-31} High-flux plasma filtration in a microfluidic environment could permit ambulatory separation of plasma from blood with a small wearable device. The recent availability of photolithographically defined pore fields^{32,33} offers a well-defined barrier with a low intrinsic membrane resistance that can separate citrated plasma from erythrocytes.³⁴ It is the filtration medium addressed in this work.

1.1 Microfiltration Theory in Microdevices

The fundamental problem in any continuous crossflow filtration system is keeping the filter clear of the retentate which is left behind as the filtrate passes through. If, as usual, the feed passes in shear flow over the filter, it must carry the retentate toward and through an exit port. Because the transverse feed velocity at the filter surface is zero, the components of the retentate must be both moved away from the filter surface and then be carried to an exit.^{35,36} All filtration theories seek to describe how this occurs. If the retentate particles are small molecules, back diffusion into the feed stream may suffice.³⁷⁻⁴⁰ If the retentate particles are larger, Brownian diffusion of retentate away from the surface will not be fast enough to sustain a reasonable filtration rate. Various authors have postulated other mechanisms for removing retentate.⁴¹⁻⁴⁶ One postulates random interactions of particles with each other and the flowing stream causing a pseudo-Brownian

movement away from the filter surface.⁴⁷ Others have postulated that a moving sludge slides over the filter toward the feed exit.^{40,48} All of these analyses presume (and hope) that the retentate will not "foul" the filter surface and its pores. When fouling occurs, temporal distinctions are in order. The foulant may quickly passivate the filter surface with possible changes in its filtration capacity, after which the system achieves a steady-state performance level. Alternatively, fouling may proceed slowly but steadily with the effect of limiting filter performance time. In the worst case, fouling simply shuts the system down.

Microfiltration has different meanings, depending on the experimental conditions.

Microfiltration becomes palpably "micro" when the retentate particles have characteristic dimensions comparable to that of the flow channel. In this circumstance, the discrete nature of the particles must be taken into account, and one may expect specific particle interactions with the filter during shear flow. With particles as large as erythrocytes in a channel not much larger than such particles, molecular diffusion is relatively unimportant and the mechanical interactions amongst particle layers become dominant.⁴⁹ For steady state to occur particles cannot accumulate at any given point. Thus, the forces which cause particles to enter a given voxel must be compensated by the forces that allow them to exit. This has been the subject of considerable inquiry.^{40,44-46,48} Considering all the details, the net effect must be that each voxel is kept in the steady state by a combination of net axial movement and the tendency for the particles to move outward due to particle interactions that overcome the forces that brought them to the membrane.^{35,36}

While the above cited studies have provided important contributions to particle motion in crossflow filtration (mostly macrofiltration), they do not translate well to filtration of soft particles in microfluidic systems, particularly under conditions that allow separation of plasma

from whole blood. Thus, the purpose of the present work is to measure the microfiltration of flowing blood in a microchannel through a recently introduced semi-conductor microsieve.³² Experiments were undertaken with the further aim of obtaining a clearer understanding of deformable particle behavior during filtration so as to enable one to predict plasma extraction from whole blood for a given set of fluidic and filter parameters.

2. Materials & Methods

2.1 Preparation of the Microsieve

All microsieves were purchased from Aquamarijn Microfiltration BV (Zutphen, Netherlands) as 500 μm thick, 5x5 or 10x20 mm^2 silicon microsieves.^{50,51} The controlling flow resistance of the sieves is a thin (<1 μm thick) layer of silicon nitride with available pore sizes of 0.25, 0.45, 0.6, 0.8, or 1.2 μm (*Figure 1*). The perforated layer is deposited on one face of the silicon backing.

The perforations are arranged in circles (membrane fields) 300 μm in diameter behind which are weep holes in the silicon support that allow filtrate to exit from its opposite side (*fig. 1.c*).

Different pore densities (10-19 million pores/sieve) and shapes (uniform circular holes or 0.6 x 2.0 μm slits) were also studied (*fig. 1.b*). Each sieve was exposed to plasma cleaning (PDC-001-HP (115V) - Harrick Plasma, Inc, Ithaca, NY) for 3 minutes at 45W (high power setting) before assembly in order to remove surface contamination and render the surface hydrophilic (contact angle <5°) to facilitate wetting. Contact angle measurements were acquired with a contact angle goniometer (Model 200 - Ramé-Hart Instrument, Inc, Succasunna, NJ).

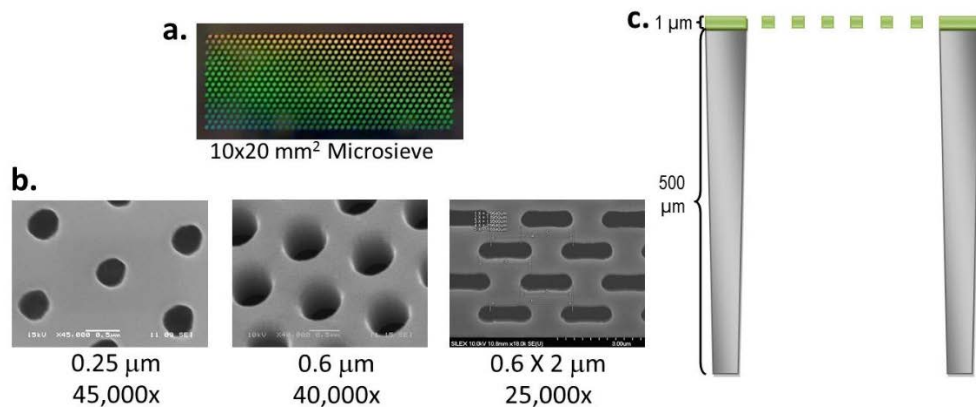


Figure 1: a) Macroscopic image of Microsieve. b) Scanning electron micrographs of microsieves with diverse pore sizes and geometries (top view), pore size depicted under each corresponding micrograph. c) Cross-sectional schematic of microsieve beneath a weep hole with the thin perforated Si_3N_4 ($<1 \mu\text{m}$) layer over the $500 \mu\text{m}$ thick silicon support.

2.2 Preparation of Blood Suspensions

Discarded packed, citrated human erythrocytes and plasma from the Columbia University Medical Center blood bank were used. Blood was reconstituted at varying hematocrits (1-33%). Because the blood components were outdated they could be expected to have undergone some deterioration. Erythrocytes were purged of cell fragments by 3 washes with Phosphate-buffered Saline (PBS) each followed by centrifugation (1000g – 15 min). The final cell layer was reconstituted with plasma that had been filtered through a $0.2 \mu\text{m}$ Millex® Syringe Filter to the desired final hematocrit.

2.3 Microfluidic Filtration Module

The filtration module consisted of three layers and three ports, as shown in *Figure 2*. The bottom layer contained the filtrate (efflux) port. The top layer contained the blood inlet and outlet. The middle layer separated the feed from the filtrate and contained the microsieve, mounted in a 0.5 mm thick frame that had been laser-cut from plastic shim-stock (Artus, Englewood, NJ). The microsieve was cemented in place with 5-Minute Instant Mix™ Epoxy (Loctite®, Inc). The height of the microfluidic feed (blood) and filtrate channels were defined by $200 \mu\text{m}$ double-sided tape (ATG type 928 double-sided transfer tape 3M, Minneapolis). The components were designed and were then cut to size by a laser cutter (Versa Laser, Scottsdale, AZ).

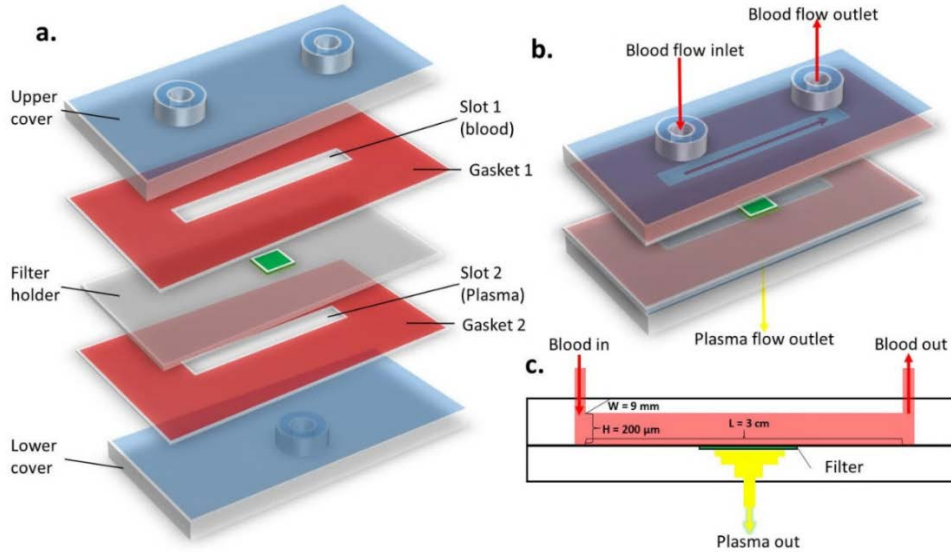


Figure 2: a) Layout of the microfluidic device. b) Semi-assembled device. c) Crossflow schematics - blood channel layer. Channel dimensions: Length (L) = 3 cm, Width (W) = 9 mm, Height (H) = 200 μm . (The actual channel height was confirmed by water pressure-flow measurements – see text, Section 2.6).

The three ports were designated P_1 , P_2 , and P_3 (Figure 3). Port 2 was connected to a feed reservoir containing either filtered saline or reconstituted blood. Permeate, the portion of liquid feed passing through the filter, flowed from P_2 to P_3 , into a 20 mL syringe whose rate of filling was controlled by a syringe pump (Legato 210p – KD Scientific, Holliston, MA). The remainder of the suspension (*i.e.* retentate) flowed out of the microchannel through P_1 into a 60 mL syringe whose rate of filling was controlled by a similar syringe pump (Legato 111 – KD Scientific, Holliston, MA). Shear rates in the device were varied from 2000-9000 s^{-1} . Filtration rates and transmembrane pressures (TMP) were measured at chosen shear rates.

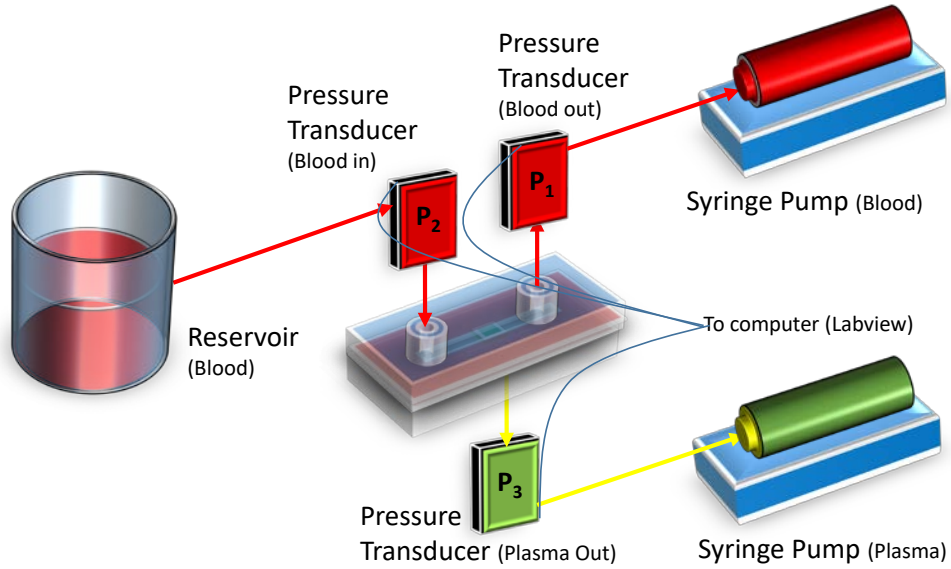


Figure 3: System arrangement including location of the pressure sensors: Blood in (P_2), Blood out (P_1), and Plasma out (P_3).

2.4 Pressure and Transmembrane Pressure (TMP) Measurements

Liquid to and from each port of the microfluidic device flowed through a pressure sensor (Utah Medical Products, Inc) connected to a data acquisition card (National Instruments cDAQ-9172, TX) that recorded each pressure history via a LabView module (National Instruments 9237, TX) (Figure 3). The transmembrane pressure (TMP) profile was computed continuously from the three pressure readings, assuming a linear variation of fluid pressure with axial distance along the channel. The LabView program used Equation 2.1:⁵²

$$TMP = \left(P_2 - \frac{1}{2}(P_2 - P_1) \right) - P_3 = \left(P_2 - \frac{1}{2}(\Delta P) \right) - P_3 \quad \text{Equation 2.1}$$

The dimensions shown in Figure 2 were used to estimate the average pressure directly above the filter surface.

2.5 Permeability of Microsieve

Prior to experiments, the intrinsic permeability of the filter was established by filtering particle-free water through the assembly. The sieves were considered to be wetted and fully open if the relationship between TMP and filtration rate was linear with a slope corresponding to the resistance of each sieve design and pore geometry, R_M (*Appendix 6.1*). R_M may be calculated experimentally as described above or from an adapted form of the Hagen–Poiseuille equation where $R = \frac{\Delta P}{Q}$ for each pore divided by the number of pores per sieve.⁵²

2.6 Microchannel Height

The thickness of the microchannel varied each time the apparatus was assembled, and had to be accurately calculated each time. By measuring the change in pressure for various through-flow rates for a fluid of known viscosity (*i.e.* microfiltered water), the half thickness (B) of the channel was calculated using the equation for laminar flow in a narrow slit solved for B :⁵²

$$B = \left(\frac{3\mu L}{2 \frac{\Delta P}{Q_m} W} \right)^{\frac{1}{3}} \quad \text{Equation 2.2}$$

The flow was assumed to be Newtonian, laminar, and fully developed, where Q_m is the volumetric flow rate, ΔP is the difference in pressure between inlet and outlet, W and L are the width and length of the channel, respectively, and μ is the viscosity of the fluid.⁵²

2.7 Shear Rate and Shear Stress at the Wall

The shear stress exerted at the flow boundaries, τ_w can be calculated by balancing the shear force at the wall against the pressure gradient for a slit channel.⁵²

$$\tau_w = \frac{\mu_s 3Q_m}{2B^2W} \quad \text{Equation 2.3}$$

Shear rates ($\dot{\gamma} = \frac{dv}{dz}$) at the wall are found as the shear stress (τ_w) divided by the viscosity:

$$\gamma_w = \frac{\tau_w}{\mu_s} = \frac{3Q_m}{2B^2W} \quad \text{Equation 2.4}$$

2.8 Post-experiment Sample Preparation

The maximum observable steady-state filtration rate was of special interest to the authors. When it was realized, an effort was made to fix the cells adherent to the surface. The system was quickly chased with PBS followed by 2% glutaraldehyde solution for 10 min (all at the same shear rate), according to Wayland's protocol.⁵³ This procedure was intended to fix adherent cells in place to allow one to investigate the behavior of erythrocyte interactions with the filtering surface as it occurred during filtration. Scanning electron micrographs were then acquired.

3. Results & Discussion

The effect of the high deformability of erythrocytes was seen throughout this work (*Figure 6*). At steady state, a significant increase in resistance to filtration was seen for all media studied regardless of pore size and shape (Section 3.2). We attribute this resistance to a stationary monolayer of erythrocytes which forms on the filter surface anchoring themselves by extension into the pores during filtration (Section 3.1, *Figure 5*). It appears that with the formation of this monolayer, the filtration resistance becomes primarily dependent on the anchored layer which, however, is seen to be incomplete (*Figures 7 and 8*). That there is any steady state filtration depends on the incompleteness of this erythrocyte monolayer.

The inflowing erythrocyte concentration (hematocrit) does not affect steady state permeation rates; it affects only their rate of approach to steady state (*Figure 8*). This incomplete layer appears to prevent further cell adherence to the sieving surface (Section 3.1). High shear flows thus appear to prevent formation of multilayers, allowing steady state filtration to be achieved (Section 3.1).

3.1 Erythrocyte Deformation during Filtration

Typical mature human erythrocytes are flexible, ovoid biconcave disks: flattened and depressed in the center, with a dumbbell-shaped cross section, and a torus-shaped rim on the edge of the disk⁵⁴ (*Figure 4.a*). Erythrocytes possess a disk diameter of approximately 6.2–8.2 μm and a thickness at the thickest point of 2–2.5 μm and a minimum thickness in the center of 0.8–1 μm .^{55,56} Overall, erythrocytes are remarkably flexible and deformable. Circulating tumor cells have also been shown to be as deformable as erythrocytes.⁵⁷ This deformability renders unique separation challenges by means of microfiltration in microdevices.

Observation of the membrane surface subsequent to filtration shows the presence of erythrocytes that have deformed and anchored themselves into filter pores. (Figs. 4.b, 6)

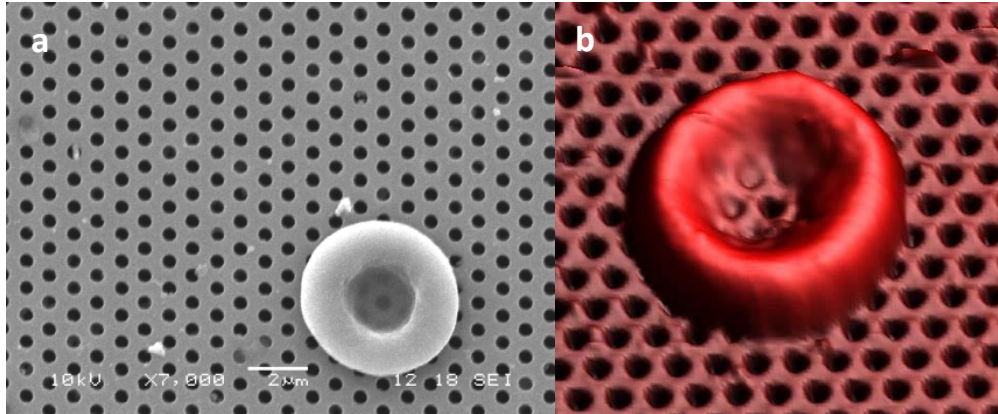


Figure 4: a) Scanning electron micrograph of a single erythrocyte on a $0.45\mu\text{m}$ microsieve retaining its biconcave shape once filtration was stopped. b) 3D enhancement with WXsM software⁵⁸ of an atomic force micrograph of a single erythrocyte, fixed with 2% glutaraldehyde, on a $0.8\mu\text{m}$ microsieve entrapped because of filtration (high TMP).

While the opacity of blood prevented direct observation of the filter surface during filtration, post-filtration observation revealed that numerous erythrocytes adhere to the pored sections of the filter surface, but not to any surrounding un-pored area (Figure 5). The buildup of particles appears to require particle deformation, a high filtration rate and correspondingly high transmembrane pressure (TMP), consistent with erythrocytes mechanically anchoring into the pores during filtration. It does not appear to depend upon reaction with the filter surface.

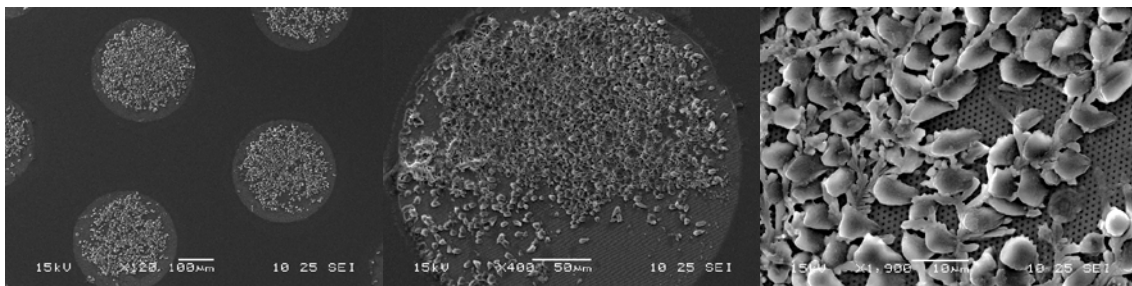


Figure 5: Scanning electron micrograph of Si_3N_4 Microsieve with 300 μm round Membrane Fields (with 0.25 μm pores) packed with “deformed” erythrocytes solely at pored regions, indicating that erythrocytes are not chemically bound to Si_3N_4 , but mechanically anchored within the pores. Measurement were made at maximum flux and high shear rate (0.35cm/min at 8000s⁻¹). Images acquired after chasing the system with 2% glutaraldehyde solution at maximum filtrate rate. Thus, the cellular behavior shown should closely approximate that during stable filtration. Magnification: 120X (L), 400X (M), 1900X (R).

When a sufficiently large fraction of the pores is blocked by anchored erythrocytes, there will be insufficient open area for additional erythrocytes to approach and anchor into the remaining open pores. Thus, a subpopulation of anchored cells prevents the remainder from being blocked and allows stable, steady-state filtration. The erythrocyte monolayer not only hinders filtrate flux but appears to provide a protected surface that allows steady state plasma filtration.

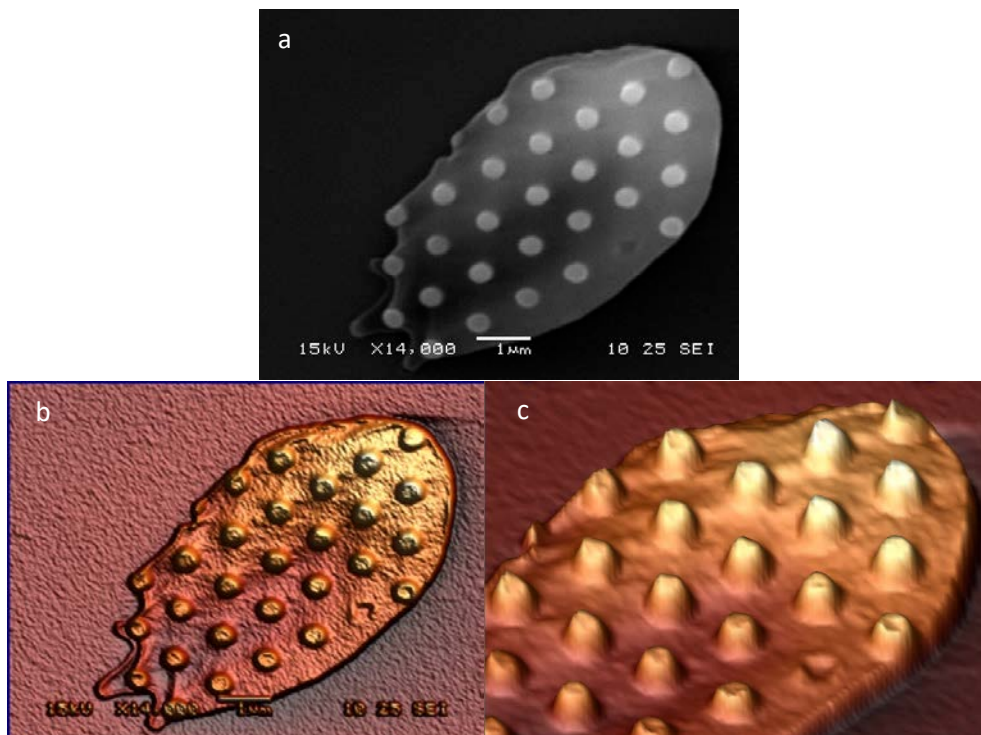


Figure 6: Scanning electron micrograph of a deformed erythrocyte that was drawn into the pores (0.25 μ m pores) during filtration and released once filtration was stopped. a) Fragment scanned at 14000X. b) Top view of the pillars. 3D enhancement with WXsM software.⁵⁸ c) 3D enhancement of b, 55 $^\circ$ view.

The percentage of pores blocked at steady state may be estimated by comparing the membrane resistance seen during filtration of filtered plasma to the steady rate of erythrocyte filtration. The latter resistance is approximately 10 times greater, suggesting that only about 10% of the pores remain open.

We postulate that this phenomenon occurs unrecognized in essentially all microfluidic devices filtering deformable particles (*e.g.* erythrocytes, circulating tumor cells). It is crucial that one accounts for its occurrence where it may prevent or, as in our case, proactively form a self-assembled biocompatible surface coating.

3.2 Quantifying the Filtration Resistance

The total filtration resistance results from contributions of the sieve and any buildup of particles:

$$R_t = \frac{\Delta P}{Q_f} = \frac{\text{TMP}}{Q_f} \quad \text{Equation 3.1}$$

Absent a cell layer, the filtration rate (Q_f) is determined by the transmembrane pressure (ΔP) and the intrinsic resistance of the sieve, quantified by filtering ultra-filtered water (Appendix: *Table I*).

Figure 7 depicts the total resistance, R_t (TMP/ Q_f), attained from Equation 3.1 using experimental measurements of TMP at the maximum stable filtration rate (Q_f) for various shear rates, and for

sieves of various porosity and pore geometry (Appendix: *Table 2*). Since pressure in a microchannel must decrease in the direction of flow, and pressure on the permeate side of a crossflow membrane is uniform, the TMP must decrease in the direction of suspension flow. This causes the maximum TMP experienced along the membrane to occur at its leading edge. If this TMP is sufficiently high, erythrocytes would be irreversibly squeezed into the membrane pores near the leading edge, causing a larger, possibly complete coverage by erythrocytes. This was directly observed on similar microsieves to be reported in a forthcoming paper.

In all cases, the total resistance (~ 33 torr/ml/min) was at least an order of magnitude greater than the sieve resistance (Appendix: *Table 1*), indicating that the total resistance was due primarily to a build-up of particles that blocked many pores on the sieve. Using different geometries and pore sizes did not lead to significantly different results. Pores ranging in size from 250 nm to 1200 nm produced about the same resistance to filtration. Even though there was approximately double the open area on the bare filter when the pores were slits in place of round holes, filtration rates were very nearly equivalent, suggesting that the total resistance at steady state is dominated by the build-up of particles, and that this build-up is independent of pore size, shape, and number.

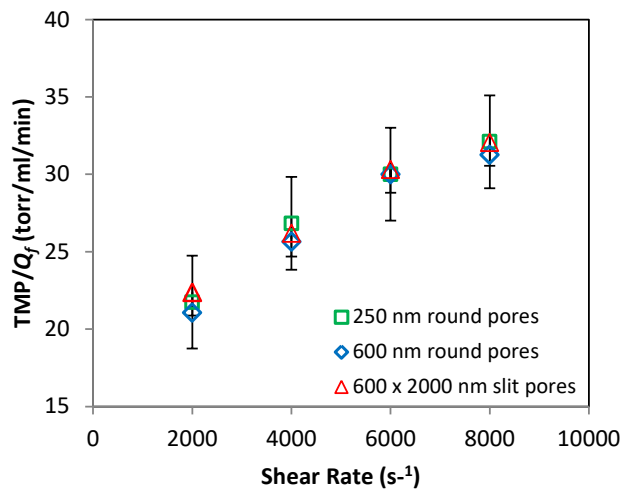


Figure 7: Experimental measurement of total resistance due to filtration and erythrocyte accumulation at the sieve surface. Filtration rate is directly proportional to shear rate. As can be seen, the maximum filtration rate at steady state is nearly the same irrespective of the pore geometry and the fraction of sieve open area.

The starting erythrocyte concentration (hematocrit) did not affect permeation (*Figure 8*) with the initial particle concentration appearing to affect the time to reach steady state but not the steady state resistance. By observing the TMP as filtration was taking place, one could visually see the TMP slowly oscillating and curving up toward steady state (*Appendix Fig. 10*). Once steady state was reached, the TMP no longer fluctuated. At higher hematocrits (45%) steady state was reached within 4-5 seconds; at lower concentrations (1%) up to 3 minutes were needed to achieve steady state at the same filtration rate. There was no effect of particle concentration on the steady states, and the transitions from one steady state to another were prompt and quicker at higher hematocrits.

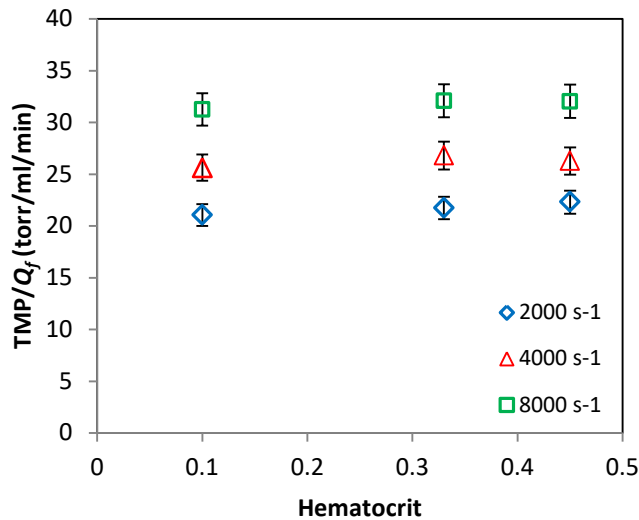


Figure 8: *The effect of hematocrit on sieve performance is not present. Contrary to classical theory, higher solute concentration was not observed to have an effect on filtration rate.*

These observations are consistent with the observed effect of initial erythrocyte concentration on the build-up of filtrate resistance. The lower the erythrocyte concentration, the fewer the cells available to plug pores as filtration ensues. Once the base erythrocyte layer is formed, the system resistance is set and is hematocrit independent (*Figures 8 and 9*).

The observation that steady state crossflow filtration of erythrocytes cannot be achieved if the TMP exceeds a “critical” value may be explained in either of two ways. Either TMP forces erythrocytes into the residual open space on the membrane surface, thereby blocking all remaining open pores, or it causes particle convection to the surface to exceed the ability of fluid forces to remove them, leading to an erythrocyte cake with zero void fraction. In this work, there seems to be substantial evidence leading toward the former, rather than latter conclusion. We conclude that the erythrocyte layer serves as an intrinsic endothelial surface that prevents

additional layering. The stable layer appears to reduce but not fully prevent plasma passage with retentate easily removed by convective diffusion above the entrapping cell layer.

4. Conclusion

The practical removal of plasma from suspended erythrocytes by filtration, using a thin silicon nitride layer photolithographically patterned with micron-sized pores was studied, with particular attention to the known hyper-flexibility of normal erythrocytes. Fouling was insensitive to pore shape and size, very sensitive to trans-filter pressure drop and surface shear rate, and remarkably insensitive to erythrocyte concentration (hematocrit). ‘Fingering’ of erythrocyte pseudopods into the membrane pores was directly imaged. Notwithstanding these phenomena, stable operating conditions were found, with a particular filter cake structure not previously described: trapped erythrocytes routinely forming an incomplete random layer that incompletely masked pores but prevented further obstruction of the pore field, thus yielding an indefinitely long-lived, stable filtering surface. In systems where trans-membrane pressure was allowed to change strongly with axial position, a ‘marching’ increase in filter resistance with time was seen and attributed to slow augmentation of cellular adhesion growing from the blood inlet.

5. Acknowledgements

Support for this work was provided in part by Grant 1R21HL088162 from the National Institute of Health, and Vizio Medical Devices, LLC. The authors also thank Columbia Medical Center Blood Bank and blood donors. We acknowledge gratefully the assistance of Dr. Robert von Gutfeld and to our whole medical team, especially Dr. Stanley Cortell and most especially the late Dr. James Jones.

6. Appendix

6.1 Nomenclature

B Half height of the channel (m)

J Permeate flux (m/s)

L Channel Length (m)

W Channel width (m)

ΔP Pressure drop across the channel (torr)

Q_F Volumetric flowrate of the permeate (*i.e.* Filtration rate) (cm³/min)

Q_m Volumetric flowrate in main channel (cm³/min)

TMP Transmembrane pressure (torr)

a Particle radius (m)

d_p Particle diameter

A_m Membrane area (m²)

n_0 number of pores per membrane

n number of open pores per membrane

F_L Lift force (N)

F_{VDW} Van der Waals force (N)

h	Distance between the particle center and the membrane surface (cm)
J_f	Filtrate flux ($\text{cm}^3/\text{cm}^2\text{-min}$)
K_L	Dimensionless constant in lift force
P	Local hydrostatic pressure (torr)
P_1	Outlet pressure (torr)
P_2	Inlet pressure (torr)
P_3	Filtrate pressure (torr)
m_p	Mass of particles in the cake (kg)
R_M	Resistance of membrane
R_L	Resistance of erythrocyte monolayer
R_C	Resistance of cake layer

Greek symbols

α	Specific resistance of cake deposit
ε	Fractional voidage of cake deposit
ρ	fluid density (kg/m^3)
γ_w	Nominal wall shear rate (1/s)

τ_w	Wall shear stress
ρ_p	Particle density
η	Viscosity of the media
μ_w	Viscosity of pure water

6.2 Supporting Data

Sieve Pore Design (μm)	Membrane Resistance ($\text{torr}\times\text{minute}/\text{cm}^3$)
0.25 round	3.39 ± 0.1
0.6 round	1.39 ± 0.1
0.6 x 2.0 slits	0.38 ± 0.05

Table 1: *Intrinsic resistance (R_M) of each membrane.*

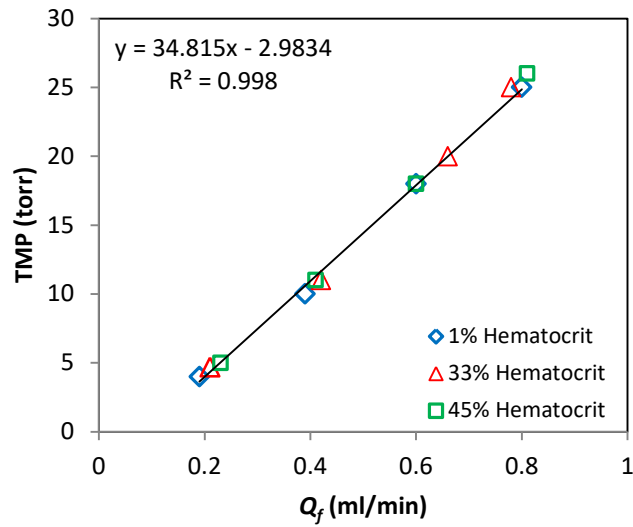


Figure 9: Maximum filtration rate is linearly dependent on shear rate (2000 - 8000 s⁻¹), however, independent of solute concentration (hematocrit) at each shear rate.

Shear Rate (s ⁻¹)	Flux (cm ³ /cm ² -min) at sub-critical TMP		
	0.25 μm round	0.6 μm round	0.6 x 2.0 μm slit
2000	0.086 ± 0.01 at 4 torr	0.104 ± 0.01 at 5 torr	0.095 ± 0.01 at 4.7 torr
4000	0.177 ± 0.01 at 10 torr	0.186 ± 0.01 at 11 torr	0.190 ± 0.01 at 11 torr
6000	0.272 ± 0.02 at 18 torr	0.272 ± 0.02 at 18 torr	0.300 ± 0.02 at 20 torr
8000	0.363 ± 0.02 at 25 torr	0.363 ± 0.01 at 26 torr	0.354 ± 0.02 at 25 torr
Sieve Pore Design	0.25 μm round	0.6 μm round	0.6 x 2.0 μm slit

Table 2: Calculated fluxes ($J = Q_f/A_m$) for each pore geometry. Q_f represents maximum filtration rate at its corresponding shear rate, and A_m corresponds to the sieving area of 2.2 cm².

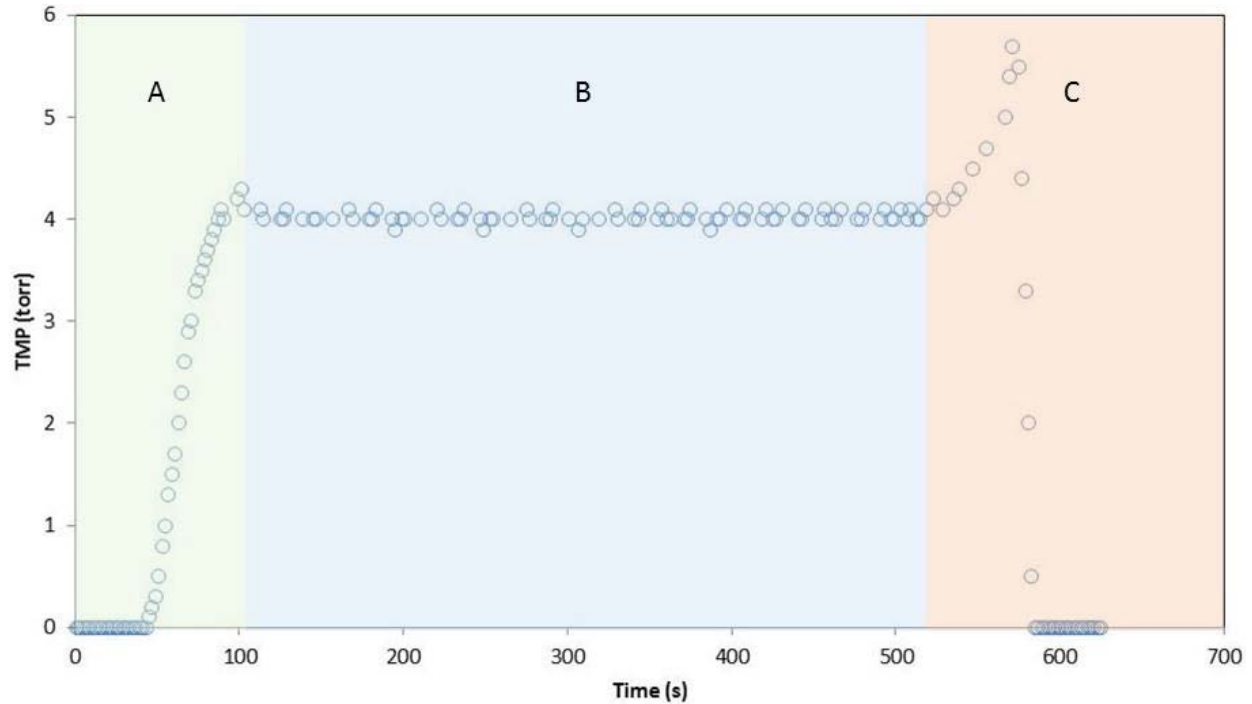


Figure 10: Transmembrane pressure profile: Initial rising slope represents the time to reach steady state (section A). Plateau represents stable filtration under subcritical TMP (section B). Steep rising represents unstable filtration with cellular accumulation and jamming of the filtering membrane when filtrate rate was increased above critical TMP (section C). TMP drops back to 0 torr when filtrate pump is stopped (at 560s).

7. References

1. Jensen KF. Microreaction engineering—is small better? *Chemical Engineering Science* 2001;56:293-303.
2. Ripperger S, Altmann J. Crossflow microfiltration—state of the art. *Separation and Purification Technology* 2002;26:19-31.
3. Yamazoe H, Okuyama T, Suzuki H, Fukuda J. Fabrication of patterned cell co-cultures on albumin-based substrate: applications for microfluidic devices. *Acta biomaterialia* 2010;6:526-33.
4. VanDelinder V, Groisman A. Separation of plasma from whole human blood in a continuous cross-flow in a molded microfluidic device. *Analytical chemistry* 2006;78:3765-71.
5. VanDelinder V, Groisman A. Perfusion in microfluidic cross-flow: separation of white blood cells from whole blood and exchange of medium in a continuous flow. *Analytical Chemistry* 2007;79:2023-30.
6. Burnouf T. Modern plasma fractionation. *Transfusion medicine reviews* 2007;21:101-17.
7. Madrigal JL, Sharma SN, Campbell KT, Stilhano RS, Gijssbers R, Silva EA. Microgels produced using microfluidic on-chip polymer blending for controlled released of VEGF encoding lentivectors. *Acta biomaterialia* 2018.
8. Silva R, Dow P, Dubay R, et al. Rapid prototyping and parametric optimization of plastic acoustofluidic devices for blood–bacteria separation. *Biomedical microdevices* 2017;19:70.
9. Carrère H, Blaszkow F, de Balmann HR. Modelling the clarification of lactic acid fermentation broths by cross-flow microfiltration. *Journal of Membrane Science* 2001;186:219-30.
10. Yeo DC, Wiraja C, Zhou Y, Tay HM, Xu C, Hou HW. Interference-free micro/nanoparticle cell engineering by use of high-throughput microfluidic separation. *ACS applied materials & interfaces* 2015;7:20855-64.
11. Sibbitts J, Sellens KA, Jia S, Klasner SA, Culbertson CT. Cellular Analysis Using Microfluidics. *Analytical chemistry* 2017;90:65-85.
12. Tolan NV, Genes LI, Subasinghe W, Raththagala M, Spence DM. Personalized metabolic assessment of erythrocytes using microfluidic delivery to an array of luminescent wells. *Analytical chemistry* 2009;81:3102-8.
13. Hu S-W, Xu B-Y, Ye W-k, Xia X-H, Chen H-Y, Xu J-J. Versatile microfluidic droplets array for bioanalysis. *ACS applied materials & interfaces* 2015;7:935-40.

14. Barata D, van Blitterswijk C, Habibovic P. High-throughput screening approaches and combinatorial development of biomaterials using microfluidics. *Acta biomaterialia* 2016;34:1-20.
15. Chen H, Cao B, Chen H, Lin Y-S, Zhang J. Combination of antibody-coated, physical-based microfluidic chip with wave-shaped arrays for isolating circulating tumor cells. *Biomedical microdevices* 2017;19:66.
16. Charcosset C. Membrane processes in biotechnology: an overview. *Biotechnology advances* 2006;24:482-92.
17. Mercier M, Maranges C, Fonade C, Lafforgue-Delorme C. Yeast suspension filtration: flux enhancement using an upward gas/liquid slug flow—application to continuous alcoholic fermentation with cell recycle. *Biotechnology and bioengineering* 1998;58:47-57.
18. Rho J, Chung J, Im H, et al. Magnetic nanosensor for detection and profiling of erythrocyte-derived microvesicles. *ACS nano* 2013;7:11227-33.
19. Rossignol N, Vandanon L, Jaouen P, Quemeneur F. Membrane technology for the continuous separation microalgae/culture medium: compared performances of cross-flow microfiltration and ultrafiltration. *Aquacultural Engineering* 1999;20:191-208.
20. Hodgson P, Leslie G, Fane A, Schneider R, Fell C, Marshall K. Cake resistance and solute rejection in bacterial microfiltration: the role of the extracellular matrix. *Journal of Membrane science* 1993;79:35-53.
21. Frenander U, Jönsson AS. Cell harvesting by cross-flow microfiltration using a shear-enhanced module. *Biotechnology and bioengineering* 1996;52:397-403.
22. Li H, Fane A, Coster H, Vigneswaran S. Observation of deposition and removal behaviour of submicron bacteria on the membrane surface during crossflow microfiltration. *Journal of Membrane Science* 2003;217:29-41.
23. Garcia-Hartjes J, Bernardi S, Weijers CA, et al. Picomolar inhibition of cholera toxin by a pentavalent ganglioside GM1os-calix [5] arene. *Organic & biomolecular chemistry* 2013;11:4340-9.
24. Al-Malack MH, Anderson G. Use of crossflow microfiltration in wastewater treatment. *Water Research* 1997;31:3064-72.
25. Peng X, Jin J, Nakamura Y, Ohno T, Ichinose I. Ultrafast permeation of water through protein-based membranes. *Nature nanotechnology* 2009;4:353-7.
26. Sollier E, Cubizolles M, Fouillet Y, Achard J-L. Fast and continuous plasma extraction from whole human blood based on expanding cell-free layer devices. *Biomedical microdevices* 2010;12:485-97.

27. Wu W-T, Martin AB, Gandini A, Aubry N, Massoudi M, Antaki JF. Design of microfluidic channels for magnetic separation of malaria-infected red blood cells. *Microfluidics and nanofluidics* 2016;20:41.
28. Martin AB, Wu W-T, Kameneva MV, Antaki JF. Development of a High-Throughput Magnetic Separation Device for Malaria-Infected Erythrocytes. *Annals of biomedical engineering* 2017;45:2888-98.
29. Dickson M, Amar L, Hill M, Schwartz J, Leonard E. A scalable, micropore, platelet rich plasma separation device. *Biomed Microdevices* 2012;14:1095-102.
30. Maria MS, Kumar B, Chandra T, Sen A. Development of a microfluidic device for cell concentration and blood cell-plasma separation. *Biomedical microdevices* 2015;17:115.
31. Rodrigues RO, Pinho D, Faustino V, Lima R. A simple microfluidic device for the deformability assessment of blood cells in a continuous flow. *Biomedical microdevices* 2015;17:108.
32. van Rijn CJ, Nijdam W, Kuiper S, Veldhuis GJ, van Wolferen H, Elwenspoek M. Microsieves made with laser interference lithography for micro-filtration applications. *Journal of Micromechanics and Microengineering* 1999;9:170.
33. Ji HM, Samper V, Chen Y, Heng CK, Lim TM, Yobas L. Silicon-based microfilters for whole blood cell separation. *Biomedical microdevices* 2008;10:251-7.
34. Dickson MN, Amar L, Hill M, Schwartz J, Leonard EF. A scalable, micropore, platelet rich plasma separation device. *Biomedical microdevices* 2012;14:1095-102.
35. Blatt WF, Dravid A, Michaels AS, Nelsen L. Solute polarization and cake formation in membrane ultrafiltration: causes, consequences, and control techniques. *Membrane science and technology*: Springer; 1970:47-97.
36. Porter MC. Concentration polarization with membrane ultrafiltration. *Industrial & Engineering Chemistry Product Research and Development* 1972;11:234-48.
37. Zydney AL, Colton CK. A Concentration Polarization Model For The Filtrate Flux In Cross-Flow Microfiltration Of Particulate Suspensions. *Chemical Engineering Communications* 1986;47:1-21.
38. Mackley MR, Sherman NE. Cross-flow cake filtration mechanisms and kinetics. *Chemical Engineering Science* 1992;47:3067-84.
39. Kromkamp J, Bastiaanse A, Swarts J, Brans G, van der Sman RGM, Boom RM. A Suspension Flow Model For Hydrodynamics And Concentration Polarisation In Crossflow Microfiltration. *Journal of Membrane Science* 2005;253:67-79.
40. Leonard EF, Vassilieff CS. The Deposition Of Rejected Matter In Membrane Separation Processes. *Chemical Engineering Communications* 1984;30:209-17.

41. Davis RH. Modeling of fouling of crossflow microfiltration membranes. *Separation and purification methods* 1992;21:75-126.
42. Sethi S, Wiesner MR. Modeling of transient permeate flux in cross-flow membrane filtration incorporating multiple particle transport mechanisms. *Journal of membrane science* 1997;136:191-205.
43. Romero CA, Davis RH. Transient model of crossflow microfiltration. *Chemical engineering science* 1990;45:13-25.
44. Segre G, Silberberg A. Behaviour of macroscopic rigid spheres in Poiseuille flow Part 1. Determination of local concentration by statistical analysis of particle passages through crossed light beams. *Journal of Fluid Mechanics* 1962;14:115-35.
45. Vasseur P, Cox R. The lateral migration of a spherical particle in two-dimensional shear flows. *Journal of Fluid Mechanics* 1976;78:385-413.
46. Drew DA, Schonberg JA, Belfort G. Lateral inertial migration of a small sphere in fast laminar flow through a membrane duct. *Chemical engineering science* 1991;46:3219-24.
47. Zydney A, Colton C. Continuous flow membrane plasmapheresis: theoretical models for flux and hemolysis prediction. *ASAIO Journal* 1982;28:408&hyphen.
48. Vassilieff CS. Convective Model Of Cross-Flow Microfiltration. *Advances in Colloid and Interface Science* 1992;40:1-36.
49. Kim M-m, Zydney AL. Particle–particle interactions during normal flow filtration: Model simulations. *Chemical Engineering Science* 2005;60:4073-82.
50. Wagdare NA, Marcelis AT, Ho OB, Boom RM, van Rijn CJ. High throughput vegetable oil-in-water emulsification with a high porosity micro-engineered membrane. *Journal of Membrane Science* 2010;347:1-7.
51. van Rijn CJ. *Nano and micro engineered membrane technology*: Elsevier; 2004.
52. Bird RB, Stewart WE, Lightfoot EN. *Transport Phenomena*: Wiley; 2007.
53. Morel FM, Baker RF, Wayland H. Quantitation of human red blood cell fixation by glutaraldehyde. *The Journal of cell biology* 1971;48:91-100.
54. Zydney AL, Saltzman WM, Colton CK. Hydraulic resistance of red cell beds in an unstirred filtration cell. *Chemical engineering science* 1989;44:147-59.
55. Canham PB. The Minimum Energy Of Bending As A Possible Explanation Of The Biconcave Shape Of The Human Red Blood Cell. *Journal of Theoretical Biology* 1970;26:61-81.

56. Yaginuma T, Oliveira MS, Lima R, Ishikawa T, Yamaguchi T. Human red blood cell behavior under homogeneous extensional flow in a hyperbolic-shaped microchannel. *Biomicrofluidics* 2013;7:054110.
57. Hou HW, Li Q, Lee G, Kumar A, Ong C, Lim CT. Deformability study of breast cancer cells using microfluidics. *Biomedical microdevices* 2009;11:557-64.
58. Horcas I, Fernández R, Gomez-Rodriguez J, Colchero J, Gómez-Herrero J, Baro A. WSXM: a software for scanning probe microscopy and a tool for nanotechnology. *Review of Scientific Instruments* 2007;78:013705.

Chapter 3

Modeling of Fouling in Cross-flow Microfiltration of Suspensions

(Published: *AIChE Journal* 65.1 (2019): 207-213)

Nopphon Weeranoppanant,¹ Levy I. Amar,^{3*} Evelyn Tong,² Monica Faria,² Michael I. Hill,²
Edward F. Leonard,^{2,3*}

¹Department of Chemical Engineering, Burapha University, Chonburi, Thailand, 20131

²Department of Chemical Engineering, ³Biomedical Engineering, Columbia University, New York, NY, USA, 10027

*Corresponding Author: Lia2103@columbia.edu, Leonard@columbia.edu – 500 West 120th street #811, New York, NY – 10027

Topical area: Separations: Materials, Devices, and Processes

Key words: microfiltration, cross-flow, suspension, pore, sieve, packed bed.

0. Abstract

Cross-flow filtration of fine suspensions through microsieves occurs in microprocessing. The interaction of particles with surfaces in microenvironments has been extensively studied, but predominantly in monolayers and not with an eye to microfiltration. Here we introduce a microfiltration model that pertains to particles that might be seen as fine in a macroscopic environment, but are large enough to intrude significantly into the shear layer of a microchannel. Thus, particle accumulation upon the sieve couples the steady-state filtrate flux and the suspension flow through the microchannel that feeds the sieve. We envision and create a stable, stationary multilayer of particles whose thickness is shear-limited and we identify and verify the structure and parameters that limit steady filtration in this environment.

At first a packed bed of particles forms, growing into and regulated by the microchannel's shear flow. A critical shear stress is shown to determine the thickness of the bed, seen as a stationary and stable multilayer of particles through which filtration may occur. As the bed thickens, at the expense of channel area for suspension flow, surface shear stress increases until no further particle adherence is possible. We built a simple example using hard non-interacting polymer microspheres and conducted cross-flow filtration experiments over Aquamarijn™ microsieves (uniform pore size of 0.8 μm). We observed a steady cake-layer thickness and because of the simple geometry afforded by uniform spheres, we could approximate the force balance, cake resistance, and filtration rate from first principles. The good fit of our data to the proposed mechanism lays a firm basis for the semi-quantitative analysis of the behavior of more complex suspensions.

1. Introduction

Recently, widespread interest in process intensification has stimulated research into applications of microfluidics for general chemical processing. Cross-flow filtration is a well-established technique that has been employed for decades to continuously separate solid-liquid mixtures.¹ While the difficulty of microfluidic solid-liquid separations has been noted,²⁻⁴ there are numerous applications in this environment that could benefit from cross-flow filtration.⁵⁻⁷ It has been successfully employed for bacterial and yeast cell harvesting,⁸⁻¹¹ as plasmapheresis for separating plasma from whole blood,^{12,13} for isolating macroscopic quantities of blood components for therapeutic purposes,^{14,15} and for non-biological applications, such as waste water recycling and latex separation.^{16,17} All of these lead to a filter cake¹⁸ comparable in size to the dimensions of the feed channel.

Despite their potential for widespread industrial and clinical use,^{15,19,20} previous models²¹⁻²⁵ for predicting filtrate flux are, in the microfluidic environment, inadequate for explaining experimental observations. Analysis of cross-flow filtration is based on the concept of a stable resistance above that offered by the filter itself,²⁶ seen as a balance between particles carried to the filter by convection, and opposed by random particle motion expressed as a diffusion-like mechanism.²⁷ The theory is based on the concept that steady state filtration is possible only when buildup and removal rates are equal, the classical concentration polarization theory.^{28,29} We have found that this theory neither depicts nor explains what is happening in a microchannel, whether filtrating water from spherical particles in aqueous suspension or plasma from red cell suspensions.^{12,26,30,31}

With particles that approach the channel size, diffusion is relatively unimportant, and the mechanical interaction of the superficial particle layer with the main flow determines a stationary and stable layer.^{32,33} Convective diffusion is important only initially, in forming the layer. Particle movements across the cake surface will be directly dependent on the shear rate and permeate flux, as observed and modeled by Knutsen and Davis for both yeast cells and latex microspheres.²⁶

In this paper, we present a new model based on shear-resistant particle immobilization on the filter surface. Microfluidic cross-flow filtration experiments demonstrate a non-negligible bed of particles building up on a filter surface.^{34,35} The layer affects not only the filtrate flux, but also the through flow of retentate.^{7,36-38} The buildup of particles is rapid, and does not depend upon fouling reactions with the filter surface.^{7,39} The model predicts filtration rates when the mechanical interactions among particles, the suspending fluid, and the filtering surface jointly control layer thickness and thus filtration. This model is shown to be in good agreement with experimental data obtained from isometric polymer beads chosen for ease of analysis.

2. Theory

Filter layers appropriate to microfluidic environments are thin, strong, and highly conductive. Resistance to filtrate flow occurs through a layer of rejected particles; and the resistance of the filter itself is unlikely to control filtrate flow. To simplify the analysis and anticipate corroborating experiments, we begin by assuming that the particle layer to be comprised of hard spheres, all of the same diameter and arranged in multiple layers within the overall filter layer. We assume no adhesive interactions.

When the filter pores have diameters not much less than the spheres above the pores, it is possible for the spheres to be held in place by the pressure differential across the filter. This immobilization will serve to block a certain fraction of the pores, generally less than unity, to a degree that depends on relative diameters, pore spacing, and how the spheres are entrapped. While the net effect of direct pore blockage is to decrease the filter permeability by the fraction of pores blocked, useful filtration often occurs in the presence of a complete particle layer. Uniform spheres will, if randomly layered on a surface until it is “jammed”, occupy at their equators 74.77% of the surface (90.69% if in ordered triangular packing). Either way, a layer of spheres leaves room for exposed filter surface because the contact area with the filter is less than the equatorial area to which the given figures apply.

Additional particles may be expected to accumulate over a base layer thus forming a stable, multilayer bed over the filter.⁴⁰ A force balance on the layer in contact with the main flow in the microfluidic channel determines the thickness of the aggregate layer. As the overall layer thickens, the channel height remaining for the main flow decreases, and the shear stress on the particle layer increases. The steady channel height is that at which the bed is just able to exert a

retaining force on a particle at the interface that is equal to the shear stress imposed on the particle by the main flow. This balance is of interest in microfluidic channels where intrusion of the particle bed into the flow channel is likely to be important.

We predict the critical shear stress, based on the geometry of an ideal isometric spherical particle bed and the filtration rate through the aggregate layer. As shown in Figure 1, components of the vertical and horizontal forces, F_v and F_h , respectively, on a particle held incipiently at the top of the packed bed at an angle of repose α will be equal and opposite. Thus:

$$F_h \cos \alpha = F_v \sin \alpha \quad \text{Equation 2.1}$$

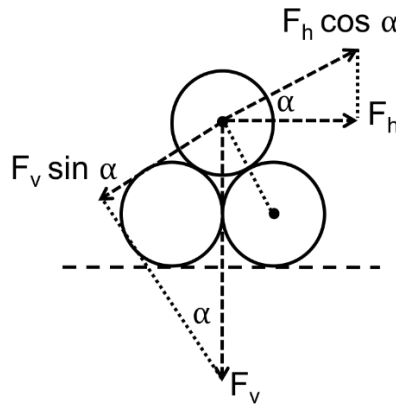


Figure 1: Forces affecting buildup of particles, where F_h is the shear force exerted by the main flow and F_v is the drag force of the filtrate flow.

Previously, White obtained an empirical expression for the horizontal force F_h , based on studies of erosion of sand beds:²⁸

$$F_h = 3.4D_p^2\tau \quad \text{Equation 2.2}$$

where D_p is the average particle diameter and τ is the shear stress at the top of the bed of particles. We define this stress as the critical shear stress (τ_c), so that:

$$F_h = 3.4D_p^2\tau_c \quad \text{Equation 2.3}$$

An expression for the vertical force on the particle bed, F_v , may be developed from the Blake-Kozeny equation for flow through packed columns:

$$\frac{P_0 - P_L}{L} = 150 \frac{\mu v_0}{D_p^2} \frac{(1-\varepsilon)^2}{\varepsilon^3} \quad \text{Equation 2.4}$$

where P_0 and P_L are the pressures at the top and bottom of the packed column, respectively, μ is the fluid viscosity, v_0 is the fluid superficial velocity, and ε is the void fraction of the bed.

Assuming this pressure drop to develop uniformly in the direction of the flow, one obtains:

$$-\frac{dp}{dz} = 150 \frac{\mu v_0}{D_p^2} \frac{(1-\varepsilon)^2}{\varepsilon^3} \quad \text{Equation 2.5}$$

The pressure on the surface of any particle at the top of the bed as a function of position along that particle may be found by describing the particle in spherical coordinates as shown in Figure 2.

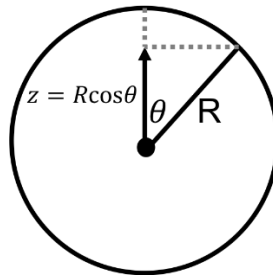


Figure 2: Transformation to spherical coordinates, where $R = D_p / 2$.

$z = R \cos \theta$, and thus $dz = -R \sin \theta d\theta$. Equation 2.5 then is transformed into:

$$\frac{dp}{d\theta} = \frac{75}{D_p} \mu v_0 \frac{(1-\varepsilon)^2}{\varepsilon^3} \sin \theta \quad \text{Equation 2.6}$$

Integrating the resulting ordinary differential equation gives:

$$\int_{p_0}^p dp = \frac{75}{D_p} \mu v_0 \frac{(1-\varepsilon)^2}{\varepsilon^3} \int_0^\theta \sin \theta d\theta \Rightarrow p(\theta) = p_0 + 75 \frac{\mu v_0}{D_p} \frac{(1-\varepsilon)^2}{\varepsilon^3} \cos \theta - 1 \quad \text{Equation 2.7}$$

where p_0 is the pressure at the top of the bed, and θ is an angle measured from a line perpendicular to the plane of the filter and passing through the center of a particle at the fluid surface. The vertical component of the corresponding normal force may be integrated over the entire surface of the particle to find the total vertical force on that particle:

$$F_v = \int_0^{2\pi} \int_0^\pi (p \cos \theta) R^2 \sin \theta d\theta d\varphi = 25 \pi \mu v_0 D_p \frac{(1-\varepsilon)^2}{\varepsilon^3} \quad \text{Equation 2.8}$$

When the two expressions for F_h and F_v are substituted into the force balance, the critical stress τ_c is found to be:

$$\tau_c = \frac{23 \mu v_0}{D_p} \frac{(1-\varepsilon)^2}{\varepsilon^3} \tan \alpha \quad \text{Equation 2.9}$$

For a particle held incipiently at the top of the bed, the critical stress varies with the fluid viscosity, the fluid superficial velocity (which by mass balance must equal the filtrate flux), the packing angle, α (Fig. 1), the particle diameter, and the bed porosity. Since fluid viscosity, particle diameter, and packing angle are typically constant for a given system, and the bed porosity will generally be within a narrow range, one expects the critical shear stress to be directly proportional to the filtrate flux. The experiments described below verify this dependence.

3. Materials and Methods

3.1 Preparation of the Microsieve

All microsieves were purchased from Aquamarijn, BV, Zutphen, Netherlands as 5mm by 5mm silicon nitride microsieves with a uniform pore size of 0.8 μm and a thickness of 700 μm . The controlling flow resistance of the sieves is a layer of silicon nitride approximately 1 μm thick. The perforations are arranged in circles approximately 300 μm in diameter behind which are weep holes that allow filtrate to exit from the opposite side of the sieve. It is necessary to ‘wet out’ the filter to overcome its hydrophobicity. Each sieve was exposed to plasma cleaning (PDC-001-HP (115V) - Harrick Plasma, Inc, Ithaca, NY) at approximately 200 mTorr for 3 minutes at 45W (high power setting) before assembly in order to remove surface contamination and render the surface hydrophilic (contact angle $<5^\circ$) to facilitate wetting. Contact angle measurements were acquired with a contact angle goniometer (Model 200 - Ramé-Hart Instrument, Inc, Succasunna, NJ).

3.2 Preparation of 5% w/w Bead Suspensions

Latex microspheres suspensions of two separate diameters (3.2 μm and 7.9 μm) were purchased from Thermo Scientific at 10% w/w concentration. All experiments were conducted with one or the other of these suspensions. The spheres were diluted to 5% w/w with deionized (DI) water and stored at room temperature. Immediately prior to each experiment, the solution was gently inverted to re-suspend the microspheres and was then exposed to a sonicator (Branson 2510, Danbury, CT) for 1 minute in order to dislodge bubbles and break up loose agglomerates.

3.3 Microfluidic Filter Body

The filter body consisted of three layers and three ports, as shown in Figure 3. The bottom metal layer contained the microsieve, mounted in a frame 0.5 mm thick that had been cut from plastic shim-stock (Artus, Englewood, NJ) using cyanoacrylate adhesive (Devcon, Inc). The middle layer was an open frame cut from 200 μm double-sided tape (ATG type 928 double-sided transfer tape 3M, Minneapolis). The top layer was a clear cover cut from 3 mm polycarbonate sheet stock (McMaster, Inc). The components were cut to size by a laser cutter (VersaLASER, Scottsdale, AZ.).

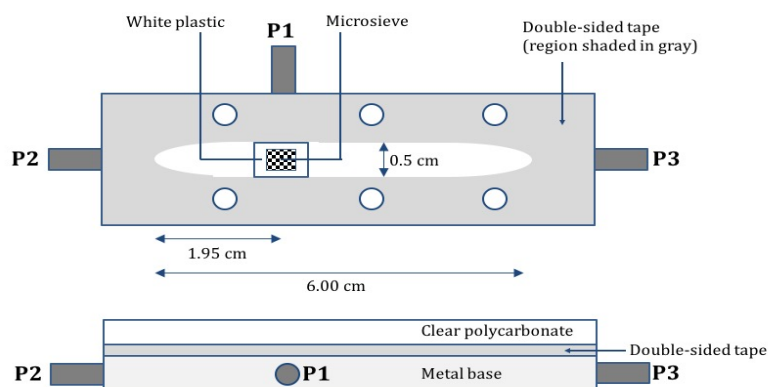


Figure 3: Layout of the microfluidic device, top and side views.

The device's three ports were designated P1, P2, and P3 (Figure 3). P2 was connected to the feed reservoir containing either filtered water or the bead suspension. Permeate, the portion of liquid feed passing through the filter, flowed from P2 to P1, into a 3 mL syringe whose rate of filling was controlled by a syringe pump (New Era Pump Systems, Wantagh, NY). The remaining fraction of the suspension (*i.e.* retentate) flowed out of the microchannel through P3 into a 60 mL syringe whose rate of filling was controlled by a similar syringe pump (Harvard Apparatus, Holliston, MA).

After assembling the microchannel, and before attaching the middle and top layers, a test was conducted to ensure that the system was closed. A 3 mL syringe was connected to P1 (Figure 3) and several drops of filtered water were added to cover the entire surface of the microsieve and surrounding white plastic shim. The syringe was pushed inward to see whether bubbles emerged from any of the device' sealed edges. If bubbles appeared, additional cyanoacrylate adhesive was applied. If bubbles were detected on the microsieve, its pore structure was judged to have been breached and was replaced. If no bubbles were seen, the device was judged ready for wetting.

To wet the filter, the 3 mL syringe was pulled outward, so that filtered water flowed through the pores until no further bubbles were seen. After the wetting step, the double-sided tape whose nominal thickness was 200 μm and which had been cut to the dimensions shown in Figure 3 was attached to the assembly. The clear plastic cover was then attached.

3.4 Pressure and Transmembrane Pressure (TMP) Measurements

The liquid from each port flowed through a pressure sensor (Utah Medical Products, Inc) connected to a data acquisition card (National Instruments cDAQ-9172, TX) that sent signals to generate the pressure history of each port in a LabView module (National Instruments 9237, TX). The transmembrane pressure (TMP) profile was computed from the three pressure readings in the LabView program using Equation 3.1:

$$\text{TMP} = \left(P_2 - \frac{1.95}{6.00} (P_2 - P_3) \right) - P_1 \quad \text{Equation 3.1}$$

Where P_1 , P_2 , and P_3 are fluid pressures at ports P1, P2, and P3, respectively. A linear variation of fluid pressure with axial distance along the channel was assumed, and the dimensions shown in Figure 3 were used in order to estimate the pressure directly above the filter surface.

3.5 Permeability of Microsieve

Prior to the experiment, the permeability of the filter was determined by the filtration of DI water through the assembly. If the relationship between TMP and filtration rate was linear with a slope less than 11.0 (torr \times min/cm³), the filter was considered to be wetted and fully open.

4. Calculations

4.1 Thickness of the Microchannel

The actual thickness of a microchannel was calculated by monitoring pressure drop during the laminar flow of particle-free water assuming the channel to be a narrow slit formed by two parallel walls of width W separated by a distance $2B$, and using the slit analog of the Hagen-Poiseuille equation:

$$Q_m = \frac{2(P_2 - P_3)B^3W}{3\mu_w L} \quad \text{Equation 4.1}$$

The slit height of the microchannel varied from one assembly to another and had to be calculated each time by solving Equation 4.1 for B :⁴¹

$$B = \left(\frac{3\mu L}{2 \frac{\Delta P}{Q_m} W} \right)^{1/3} \quad \text{Equation 4.2}$$

where Q_m is the main volumetric flowrate, ΔP is the difference between P_2 and P_3 , B is the half thickness of the channel, W and L are the width and length of the channel, and μ is the viscosity of the fluid.

4.2 Viscosity of Particle Suspension

The effective viscosity of the particle suspension, μ_s , was determined by solving Equation 4.1 using the measured pressure drop and the previously determined thickness values of x , B , and W at each Q_m to give:

$$\mu_s = \frac{2B^3W}{3L} \frac{\Delta P}{Q_m}$$

Equation 4.3

The ratio $\Delta P/Q_m$ was employed, as determined from a plot of pressure drop versus flow in the channel.

4.3 Shear Stress at the Wall

The shear stress exerted at the flow boundaries is calculated as the product of viscosity and the shear rate at the boundaries. The boundary on which filtration occurs extends inward from the filter surface by a distance x , reducing the total slit height to $2B - x$. The shear stresses on each boundary are equal:

$$\tau = \mu_s \gamma = \frac{\mu_s 3Q_m}{2 \left(B - \frac{x}{2} \right)^2 W}$$

Equation 4.4

4.4 Thickness of the Particle Packed Bed

The presence of a packed bed increases the pressure drop along the microchannel. This pressure drop can be written as the sum of three pressure drops for three axial regions: (a) from the inlet to the filter, (b) across the filter, and (c) from the filter to the outlet.

- i. When no filtration is applied (and thus no particle layer is formed):

$$\Delta P = \Delta P_a + \Delta P_b + \Delta P_c$$

Equation 4.5

- ii. During filtration

$$\Delta P' = \Delta P_a' + \Delta P_b' + \Delta P_c'$$

Equation 4.6

where the prime symbols designate the data obtained when filtration is imposed.

Thus, the increase in pressure drop due to a layer of packed bed is estimated by subtracting a pressure drop at no filtration from a pressure drop during filtration. It is assumed that the pressure drop in regions other than the filter surface stay constant ($\Delta P_1 = \Delta P'_1$ and $\Delta P_2 = \Delta P'_2$).

Hence the thickness of the packed bed was calculated by solving for x in the following equation:

$$\Delta P - \Delta P' = \Delta P_b - \Delta P'_b = \frac{3\mu_s L Q_m}{2B^3 W} - \frac{3\mu_s L Q_m}{2(B - \frac{x}{2})^3 W} \quad \text{Equation 4.7}$$

5. Results and Discussion

5.1 Minimum Main Flowrate yielding stable TMP at a Given Filtration Flowrate

Steady state is indicated by a stable TMP, and it occurs when components of the shear force $F_h \cos \alpha$, and drag force, $F_v \sin \alpha$, on the edge of the packed bed are balanced, as described in Equation 2.1. If the two force components are not balanced, the system remains in a transient state, and the thickness of the bed either increases or decreases, demonstrated experimentally by a changing TMP. As discussed by Aiman and Howell, variations of permeate flux can significantly alter the condition in the boundary layer.³⁷ Therefore, in this work we maintained the flux (*i.e.* the filtration rate) constant and measured TMP. The TMP profile was interrogated to obtain information about the packed bed formation.

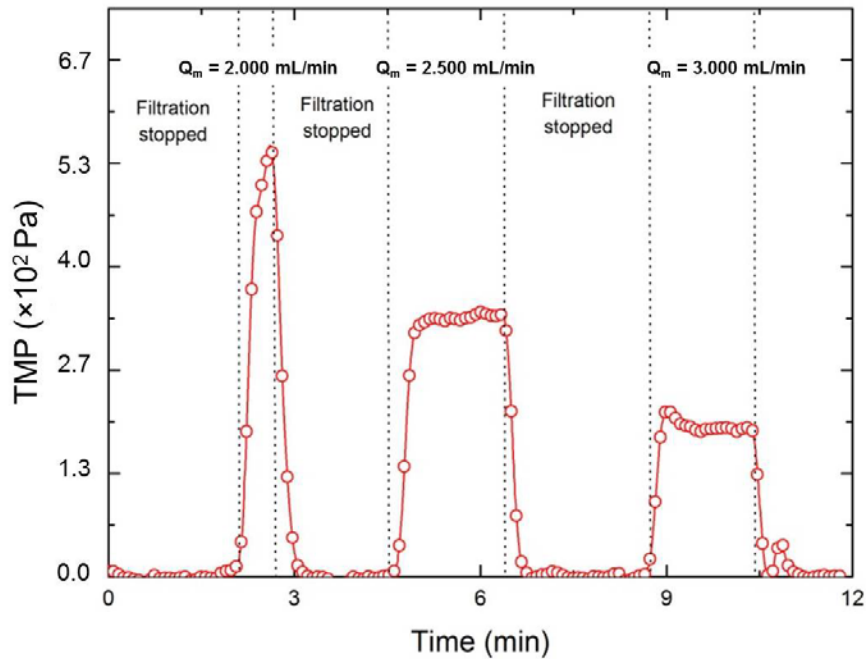


Figure 4: Sample transmembrane pressure (TMP) profile, given a filtration flowrate of 0.020 mL/min, for various main flowrates (Q_m).

We use Q_f to denote the filtration rate. At each Q_f , a minimum main flowrate $Q_{m,min}$ was defined as the lowest value of Q_m to maintain a stable TMP. Figure 4 displays TMP using different Q_m 's but a fixed value of Q_f . As shown in Figure 4, at Q_m of 2.000 mL/min, the TMP was unstable, but when Q_m was increased to 2.500 and 3.000 mL/min, the TMP profile leveled off, connotating a stable TMP and steady filtration. Therefore, $Q_{m,min}$ was approximated as 2.500 mL/min. The values of $Q_{m,min}$ for other conditions (*e.g.* different bead sizes, Q_f) are summarized in Table 1.

Q_f , mL/min	$Q_{m,min}$, mL/min	
	3.2 μ m beads	7.9 μ m beads
0.010	1.500	0.500
0.020	2.500	1.000
0.030	3.500	2.200

Table 1: $Q_{m,min}$ at different filtration rates (Q_f) for two different particle sizes.

As we increase Q_f , $Q_{m,min}$ increases. A higher value of Q_f implies a stronger drag force, which then requires a larger shear force derived from the main flowrate to maintain steady state. $Q_{m,min}$ decreases with larger particle sizes. This agrees with expectation that the shear force varies with the square of particle diameter, whereas the drag force is only proportional to particle diameter. Thus, as particle diameter increases, the shear force dominates and requires a smaller $Q_{m,min}$ to maintain steady state.

5.2 Packed Bed Thickness and Porosity

The packed bed thickness was determined from the difference in channel height (B) without filtration (Equation 4.1), and with filtration (Equation 4.7). The assumption here was that for a given Q_m , any change in TMP during filtration was entirely due to the packed bed formation. Equation 5.1 was used to solve for the effective half-height of the channel in the presence of a packed bed layer,⁴¹ where L is the length of the main channel while x is the thickness of the packed bed.

$$\left(B - \frac{x}{2}\right)^3 = \frac{3B^3 \mu_s L Q_m}{3\mu_s L Q_m - 2(TMP - TMP')WB^3} \quad \text{Equation 5.1}$$

The packed bed thickness increases with decreasing Q_m due to a weaker shear force along the channel. We also observed that an increased in Q_f increased the packed bed thickness. This was in agreement with our hypothesis that the drag force would increase the number of particles building up as layers on the filter. However, changes in drag force became less significant when filtration rate (Q_f) was above 0.020 mL/min, as evidenced by similar bed thicknesses at $Q_f = 0.020$ and $Q_f = 0.030$ mL/min. At this point, the drag force would lead to denser packing in

place of forming more layers. The packed bed thicknesses at different values of Q_f and Q_m are summarized in Figure 5.

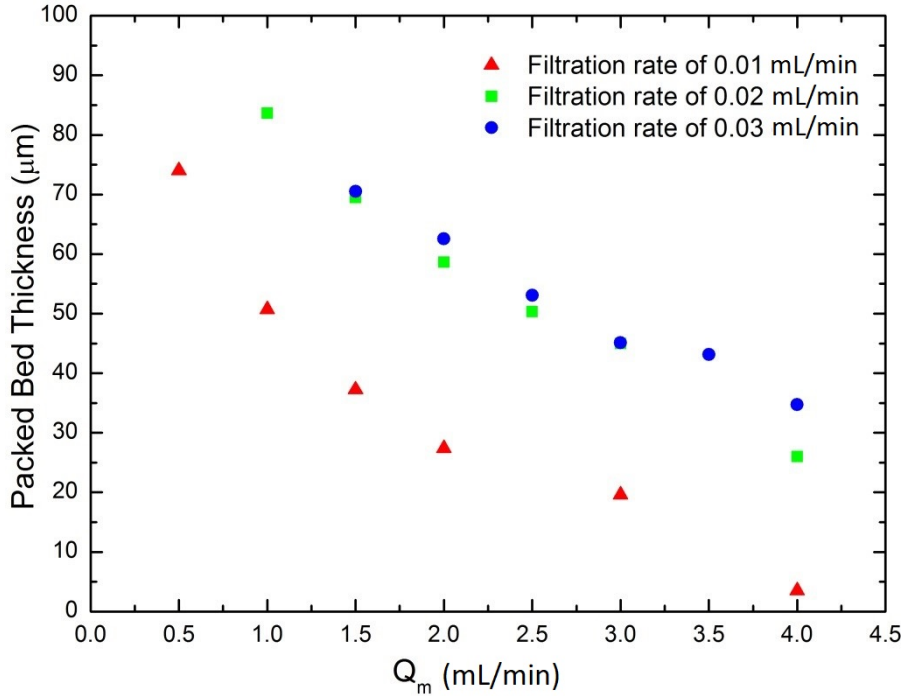


Figure 5: Packed bed thickness as a function of Q_m and Q_f using $7.9 \mu\text{m}$ bead suspension.

Packed bed thickness decreases as a function of Q_m and increases as a function of Q_f .

For each data set, the Blake-Kozeny calculation of packed bed porosity is applied to test the experimental data. Since the packed bed is incompressible, assuming the porosity to be independent of the imposed differential pressure.⁴² The porosity intrinsic to the sphere geometry, ϵ , is reported to be as 0.35-0.45.³⁵

$$\frac{TMP}{L} = 150 \left(\frac{\mu_w v_o}{D_p^2} \right) \frac{(1-\epsilon)^2}{\epsilon^3} \quad \text{Equation 5.1}$$

Table 2 shows that the porosity obtained from the experimental data set is consistent, and in agreement with the reported value.

Q_m (mL/min)	Porosity
3.600	0.34
3.700	0.33
3.800	0.33
3.900	0.33
4.000	0.30

Table 2: Calculated porosity using the Blake-Kozeny equation for $Q_f = 0.030$ mL/min at varying Q_m .

5.3 Critical Shear Stress

We define a critical shear stress τ_c , as the minimum sweeping force at the filter surface necessary to prevent formation of the packed bed. If the shear stress exerted by cross-flow filtration is greater than τ_c , no packed bed will form. If the shear stress is smaller than τ_c , the packed bed will build up and narrow the microchannel until the shear stress at the surface of the packed bed is equal to τ_c . At this point, we expect the packed bed to become stable and cease growing.

Table 3 demonstrates the steady state achieved at Q_m of 3.6 mL/min, indicative of the constant wall shear stress at the surface of the packed bed (for 3.2 μm particle size and filtration rate 0.030 mL/min).

Q_m (mL/min)	Wall Shear Stress (Pa)
3.600	4.10
3.700	4.24
3.800	4.11
3.900	4.20
4.000	4.10

Table 3: Calculated wall shear stress of filtrations at constant $Q_f = 0.030$ mL/min for varying Q_m .

The critical shear stress (τ_c) was calculated using Equation 4.3. Values of τ_c for two particle sizes (3.2 μm 7.9 μm in diameter) are summarized in Table 4.

Q_f , mL/min	τ_c (Pa)	
	3.2 μm beads	7.9 μm beads
0.010	1.50 \pm 0.30	0.80 \pm 0.23
0.020	3.00 \pm 0.89	1.63 \pm 0.52
0.030	4.37 \pm 1.27	2.47 \pm 0.64

Table 4: Average critical shear stress (τ_c) at different filtration rates (Q_f) for two different sizes of particles used. The critical shear stress increased with filtration rate. Smaller bead results in higher critical shear stress.

Particle size has a large effect on critical shear stress, as evidenced by the critical shear stress for 3.2 μm beads being almost double that for the 7.9 μm beads at the same filtrate flowrate. Another important trend is that the critical shear stress is linearly related to Q_f for the regimen of shear flow analyzed, as shown in Figure 6. It is, thus, possible to predict the critical shear stress given a filtrate flowrate using a linear fit.

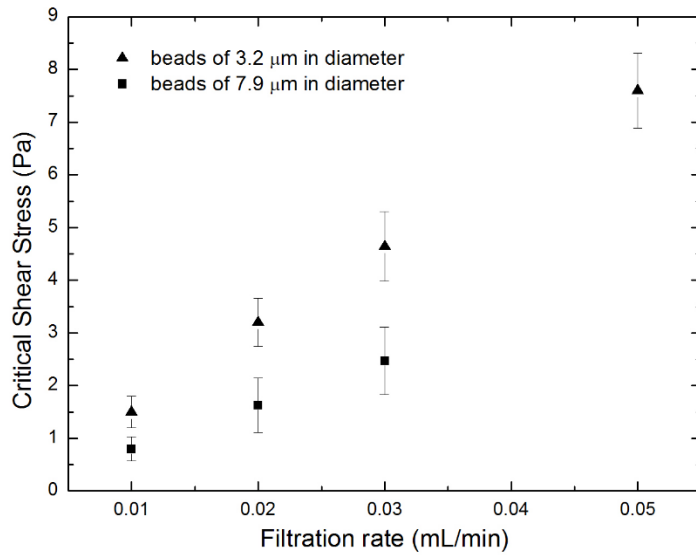


Figure 6: Critical shear stress versus filtrate flowrate for various bead diameters. Critical shear stress at each filtration rate (Q_f) was plotted to demonstrate a monotonically increasing trend, aligned with our theoretical prediction.

A further, qualitative observation corroborates the proposed mechanism and distinguishes it from a diffusion-based explanation of particle accumulation. For the dilute range of particle

concentration studied here, there was no effect of particle concentration on the steady-states discussed here and the transitions from one steady state to another were prompt and quicker at higher particle concentrations when layer thickness was increasing because particles were being delivered more quickly. No permanent fouling was observed.

6. Conclusion

Cross-flow (tangential) microfiltration of uniform beads in solution can be modeled and interpreted as a simple force balance at the interface between a stationary filter cake and a feed stream moving over it. For a suspension - composed of uniform, hard spherical beads - a first-principles model was built and was successfully compared with experimental data. Other systems may present a more complex interfacial geometry and pore structure. However, such systems should preserve the fundamental findings of this research: that interfacial mechanics, and not particle migration, determine the fraction of a microfilter's cross-section that is available for through-flow.

The essence of this model is that in the crowded space of a microfluidic filter, the feed flows through a narrow slit, sharing the slit height with a stationary filter cake. Thus, a self-sustaining force balance is achieved. This force balance sets and maintains a split in slit height. By measuring TMP for various filtrate and main flowrates, the minimum flowrate and critical shear stress to prevent unstable packed bed formation was found and related to main flowrate, filtrate flowrate, and particle size. A linear relationship was found between critical wall shear stress and filtrate flowrate, an inverse relationship between particle size and critical wall shear stress, and no relationship between the main flowrate and the critical wall shear stress, all in support of the proposed model.

One cannot expect such clear and simple relationships for particles that are more complex in shape and size. However, the underlying phenomenology is likely to be preserved and to provide a basis for understanding and correlating observations in such systems. Further work will be needed to analyze less uniform particle beds.

7. Acknowledgements

Support for this work was provided in part by Grant 1R21HL088162 from the National Institute of Health, and from Vizio Medical Devices, LLC.

8. Notation

Variables

B	Half height of the channel (μm)
D_p	Diameter of spherical particles (μm)
F_h	Horizontal force on the particle (N)
F_v	Vertical force on the particle (N)
L	Length of the channel (cm)
ΔP	Pressure across the entire channel (Pa)
Q_f	Volumetric flowrate of the permeate (i.e. Filtration rate) (mL/min)
Q_m	Volumetric flowrate along the main channel (mL/min)
Q_m	Volumetric flowrate along the main channel (mL/min)
$Q_{m, min}$	Minimum volumetric flowrate along the main channel required to maintain a stable TMP profile (mL/min)
TMP	Transmembrane pressure (Pa)
v_o	Filtration velocity or fluid superficial velocity (cm/s)
W	Width of the channel (cm)
x	Thickness of packed bed (μm)

Greek letters

γ	Shear rate (s^{-1})
τ	Shear stress (Pa)
τ_c	Critical shear stress (Pa)
μ	Viscosity of fluid (Pa.s)
μ_w	Viscosity of DI water (Pa.s)

μ_s Viscosity of bead suspension (Pa.s)
 α Angle of repose (radian)
 ε Void fraction of packed bed (%)

9. References

1. Ripperger S, Altmann J. Crossflow microfiltration—state of the art. *Sep Purif Technol.* 2002;26:19-31.
2. Cakl J, Mikulášek P. Flux and Fouling in the Crossflow Ceramic Membrane Microfiltration of Polymer Colloids. *Sep Sci Technol.* 1995;30:3663-80.
3. Davis RH. Modeling of fouling of crossflow microfiltration membranes. *Sep Purif Methods.* 1992;21:75-126.
4. Gutierrez-Rivera L, Katekawa M, Silva M, Cescato L. Characterization of the selectivity of microsieves using a cross-flow microfiltration system. *Brazilian J Chem Eng.* 2010;27:677-85.
5. Jensen KF. Microreaction engineering—is small better? *Chem Eng Sci.* 2001;56:293-303.
6. Belfort G, Davis RH, Zydney AL. The behavior of suspensions and macromolecular solutions in crossflow microfiltration. *J Memb Sci.* 1994;96:1-58.
7. Di H, Martin GJ, Dunstan DE. A microfluidic system for studying particle deposition during ultrafiltration. *J Memb Sci.* 2017;532:68-75.
8. Tanaka T, Tsuneyoshi S-I, Kitazawa W, Nakanishi K. Characteristics in crossflow filtration using different yeast suspensions. *Sep Sci Technol.* 1997;32:1885-98.
9. Crespo J, Xavier A, Barreto M, Gonçalves L, Almeida J, Carrondo M. Tangential flow filtration for continuous cell recycle culture of acidogenic bacteria. *Chem Eng Sci.* 1992;47:205-14.
10. Li H, Fane A, Coster H, Vigneswaran S. Observation of deposition and removal behaviour of submicron bacteria on the membrane surface during crossflow microfiltration. *J Memb Sci.* 2003;217:29-41.
11. Wu W-T, Martin AB, Gandini A, Aubry N, Massoudi M, Antaki JF. Design of microfluidic channels for magnetic separation of malaria-infected red blood cells. *Microfluidics Nanofluidics* 2016;20:41.
12. Zydney A, Colton C. Continuous flow membrane plasmapheresis: theoretical models for flux and hemolysis prediction. *ASAIO Journal* 1982;28:408.
13. Zydney A, Colton C. A red cell deformation model for hemolysis in cross flow membrane plasmapheresis. *Chem Eng Commun.* 1984;30:191-207.
14. Dickson M, Amar L, Hill M, Schwartz J, Leonard E. A scalable, micropore, platelet rich plasma separation device. *Biomed Microdevices* 2012;14:1095-102.

15. Malchesky PS. Membrane Processes for Plasma Separation and Plasma Fractionation: Guiding Principles for Clinical Use. *Therapeutic Apher.* 2001;5:270-82.
16. Ahmad AL, Lah C, Fahanis N, Ismail S. Ultrasonically Aided Cross-flow Membrane Filtration for Latex Wastewater. *J Phys Sci* 2018;29.
17. Manouchehri M, Kargari A. Water recovery from laundry wastewater by the cross flow microfiltration process: A strategy for water recycling in residential buildings. *J Cleaner Production* 2017;168:227-38.
18. Di H, Martin GJ, Sun Q, Xie D, Dunstan DE. Detailed, real-time characterization of particle deposition during crossflow filtration as influenced by solution properties. *J Memb Sci.* 2018;555:115-24.
19. Singh V, Purkait M, Das C. Cross-flow microfiltration of industrial oily wastewater: Experimental and theoretical consideration. *Sep Sci Technol.* 2011;46:1213-23.
20. Joshi S, Pellacani P, van Beek TA, Zuilhof H, Nielen MW. Surface characterization and antifouling properties of nanostructured gold chips for imaging surface plasmon resonance biosensing. *Sensors Actuators B: Chemical* 2015;209:505-14.
21. Bacchin P, Si-Hassen D, Starov V, Clifton MJ, Aimar P. A unifying model for concentration polarization, gel-layer formation and particle deposition in cross-flow membrane filtration of colloidal suspensions. *Chem Eng Sci.* 2002;57:77-91.
22. Zydney A, Colton C. A concentration polarization model for the filtrate flux in cross-flow microfiltration of particulate suspensions. *Chem Eng Commun.* 1986;47:1-21.
23. Vassilieff CS. Convective model of cross-flow microfiltration. *Adv Colloid Interface Sci.* 1992;40:1-36.
24. Mattsson T, Lewis WJ, Chew YJ, Bird MR. The use of fluid dynamic gauging in investigating the thickness and cohesive strength of cake fouling layers formed during cross-flow microfiltration. *Sep Purif Technol.* 2017.
25. Makabe R, Akamatsu K, Nakao S-i. Classification and diafiltration of polydispersed particles using cross-flow microfiltration under high flow rate. *J Memb Sci.* 2017;523:8-14.
26. Knutsen JS, Davis RH. Deposition of foulant particles during tangential flow filtration. *J Memb Sci.* 2006;271:101-13.
27. Belfort G, Davis R, Zydney A. The behavior of suspensions and macromolecular solutions in cross-flow microfiltration. *J Memb Sci.* 1994;96:1-58.
28. Asaadi M, White D. A model for determining the steady state flux of inorganic microfiltration membranes. *Chem Eng J.* 1992;48:11-6.

29. Davis RH, Sherwood JD. A similarity solution for steady-state crossflow microfiltration. *Chem Eng Sci.* 1990;45:3203-9.
30. Malchesky PS, Horiuchi T, Lewandowski JJ, Nosè Y. Membrane plasma separation and the on-line treatment of plasma by membranes. *J Memb Sci.* 1989;44:55-88.
31. Makabe R, Akamatsu K, Nakao Si. Limiting flux in microfiltration of colloidal suspensions by focusing on hydrodynamic forces in viscous sublayer. *AIChE J.* 2018;64:1760-5.
32. Levesley JA, Bellhouse BJ. Particulate separation using inertial lift forces. *Chem Eng Sci.* 1993;48:3657-69.
33. Wang W, Jia X, Davies GA. A theoretical study of transient cross-flow filtration using force balance analysis. *Chem Eng J Biochem Eng J.* 1995;60:55-62.
34. Tarabara VV, Hovinga RM, Wiesner MR. Constant transmembrane pressure vs. constant permeate flux: effect of particle size on crossflow membrane filtration. *Env Eng Sci.* 2002;19:343-55.
35. Smith WO, Foote PD, Busang PF. Packing of homogeneous spheres. *Phys Review* 1929;34:1271-4.
36. Mackley MR, Sherman NE. Cross-flow cake filtration mechanisms and kinetics. *Chem Eng Sci.* 1992;47:3067-84.
37. Aimar P, Howell JA, Turner M. Effects of concentration boundary-layer development on the flux limitations in ultrafiltration. *Chem Eng Res Design* 1989;67:255-61.
38. Di H, Martin GJ, Sun Q, Xie D, Dunstan DE. Detailed, real-time characterization of particle deposition during crossflow filtration as influenced by solution properties. *J Memb Sci.* 2018.
39. Song L. Flux decline in crossflow microfiltration and ultrafiltration: mechanisms and modeling of membrane fouling. *J Memb Sci.* 1998;139:183-200.
40. Losey MW, Schmidt MA, Jensen KF. Microfabricated multiphase packed-bed reactors: characterization of mass transfer and reactions. *Industrial Eng Chem Res.* 2001;40:2555-62.
41. Bird RB, Stewart WE, Lightfoot EN. *Transport Phenomena*: Wiley; 2007.
42. Lightfoot EN. *Transport phenomena and living systems; biomedical aspects of momentum and mass transport.* New York,: Wiley; 1973.

Chapter 4

Co-current Crossflow Microfiltration in a Microchannel

(Accepted in Biomedical Microdevices Journal)

Levy I. Amar,^{1*} Michael I. Hill,² Monica Faria,² Daniela Guisado,² Cees J. M. van Rijn,³ Edward
F. Leonard,^{1,2*}

Department of Biomedical Engineering¹, and Chemical Engineering², Columbia University, New
York, NY – 10027

MicroFluidics and NanoTechnology/ORC⁴, Wageningen University Stippeneng, Wageningen –
6708 WE, The Netherlands

*Corresponding Author: Lia2103@columbia.edu, Leonard@columbia.edu – 500 West 120th
street #811, New York, NY - 10027

Topical area: Microfluidics, Separations: Materials, Devices, and Processes, Artificial Organs.

Key words: cross-flow, microfluidics, microfiltration model, constant transmembrane pressure,
microsieve, sieve, nanopores, blood, erythrocytes, plasma.

0. Abstract

Steady state crossflow microfiltration (CMF) is an important and often necessary means of particle separation and concentration for both industrial and biomedical processes. The factors controlling the performance of CMF have been extensively reviewed. A major factor is transmembrane pressure (TMP). Because microchannels have small height, they tend to have high pressure gradients in the feed-flow direction. In the extreme, these gradients may even reverse the pressure across the membrane (inciting backflow). It is therefore desirable to compensate for the effect of feed-flow on the TMP, aiming at constant transmembrane pressure (cTMP) at a value which maximizes filtrate flux. This is especially critical during filtration of deformable particles (*e.g.* erythrocytes) through low intrinsic resistance membranes.

Filtration flux is generally taken to be directly proportional to TMP, with pressure drop along the channel decreasing in the flow direction. A co-current flow of filtrate in a suitably designed filtrate collecting channel is shown to allow the TMP to remain constant and permit the sieving surface to perform optimally, permitting up to twice as much filtration over that of a naïve configuration. Manipulation of the filtrate channel may be even more beneficial if it prevents backflow that might otherwise occur at the end of a sufficiently long channel. Experiments with erythrocyte suspensions, reported here, validate these concepts.

1. Introduction

In crossflow microfiltration (CMF), the fluid to be filtered flows parallel to a membrane surface, allowing permeation through the membrane, driven by a pressure difference.¹ In a companion study,¹ we noted a wide range of filtration duties which can be addressed by CMF,²⁻⁶ including many medical and biotechnical applications.^{7,8} These situations generally show increasing filtration flux as transmembrane pressure (TMP) is increased until a TMP is established that apparently anchors particles to, and blocks the membrane.⁹⁻¹¹ Under ordinary conditions, (Fig. 1, column A) fouling occurs first at the inlet, where TMP is highest, with much of the filter operating below capacity because pressure drops significantly in the direction of flow.¹²⁻¹⁵ Full utilization of the membrane is possible only if TMP is held constant (cTMP) (Fig. 1, column B), just below critical flux.¹⁶

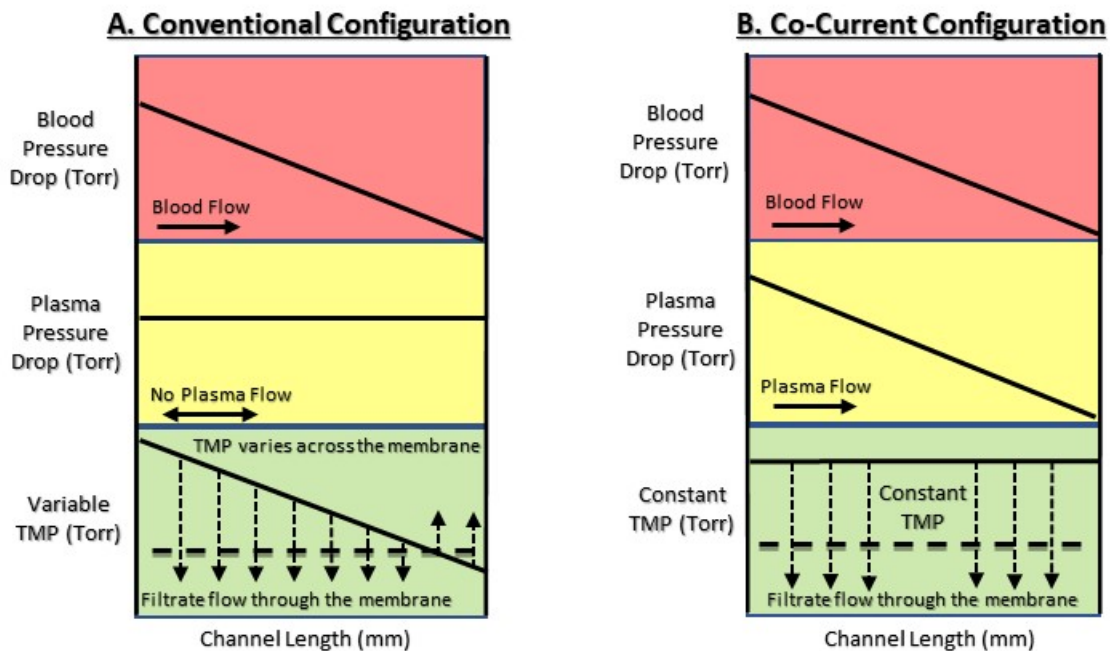


Figure 1. Pressure profiles of conventional (column A), and co-current (column B) filtration configurations. The first row (red) of the figure shows the expected pressure drop down the feed (blood)

channel. The second row (yellow) shows, left, the usual, constant pressure in the filtrate (plasma) channel, and, right, a filtrate collecting channel with plasma flow configured to establish in the channel a pressure gradient that parallels that in the feed channel. The third row (green) shows, left, how a computed transmembrane pressure (TMP) drops across the channel length to the point it can produce backflow in the presence of an invariant filtrate pressure. And (right) how a varying plasma channel pressure can produce a constant transmembrane pressure. The straight-line variation in blood pressure in all panels of the figure presumes a low ratio of filtration flow to channel flow.

Construction of an appropriate filtrate collecting channel involves specifying a cross-section, an axial flowrate, and a circulating fluid (filtrate or filtrate diluted into another fluid) specified to produce the desired axial pressure gradient. This configuration is easily achieved in dialyzer-like configurations if both the feed and filtrate flows occur in the same direction, with the filtrate flow adjusted to yield constant TMP. In this study we report achieving this configuration in a simple parallel-plate geometry, one filter, one feed with a single filtering surface, and one circulating fluid receiving the filtrate. In separate runs we varied the feed flow over a wide range of shear rates. This was done over two filtering surfaces one twice as large (long) as the other.

2. Materials & Methods

To achieve a valid comparison of constant transmembrane pressure (cTMP) with the normal parallel flow configuration, we utilized experimental methods and materials from our earlier study.¹ As described there,¹ all microsieves were purchased from Aquamarijn Microfiltration BV (Zutphen, Netherlands) as 500 μm thick, 10x20 mm^2 silicon microsieves.^{17,18} Discarded packed citrated human erythrocytes and plasma from the Columbia University Medical Center blood bank were used. The suspension used in these experiments was reconstituted with plasma that had been filtered through a 0.2 μm Millex® syringe filter to the desired final hematocrit of 33% and triply washed erythrocytes.

2.1 Microfluidic Filtration Module

The filtration module consisted of three layers and four ports, as shown in *figure 2*. The top layer contained the blood inlet and outlet. The bottom layer contained the filtrate inlet and outlet. The middle layer separated the feed from the filtrate and contained the microsieve, mounted in a 0.5 mm thick frame that had been laser-cut from plastic shim stock (Artus, Englewood, NJ). The microsieve was cemented in place with 5-Minute Instant Mix™ Epoxy (Loctite®, Inc). The height of the microfluidic feed (blood) and filtrate (plasma) channels were defined by 200 μm and 100 μm thick double-sided tapes, respectively (ATG type 928, and 924 double-sided transfer tape, 3M, Minneapolis). The components were designed and were then cut to size by a laser cutter (Versa Laser, Scottsdale, AZ).

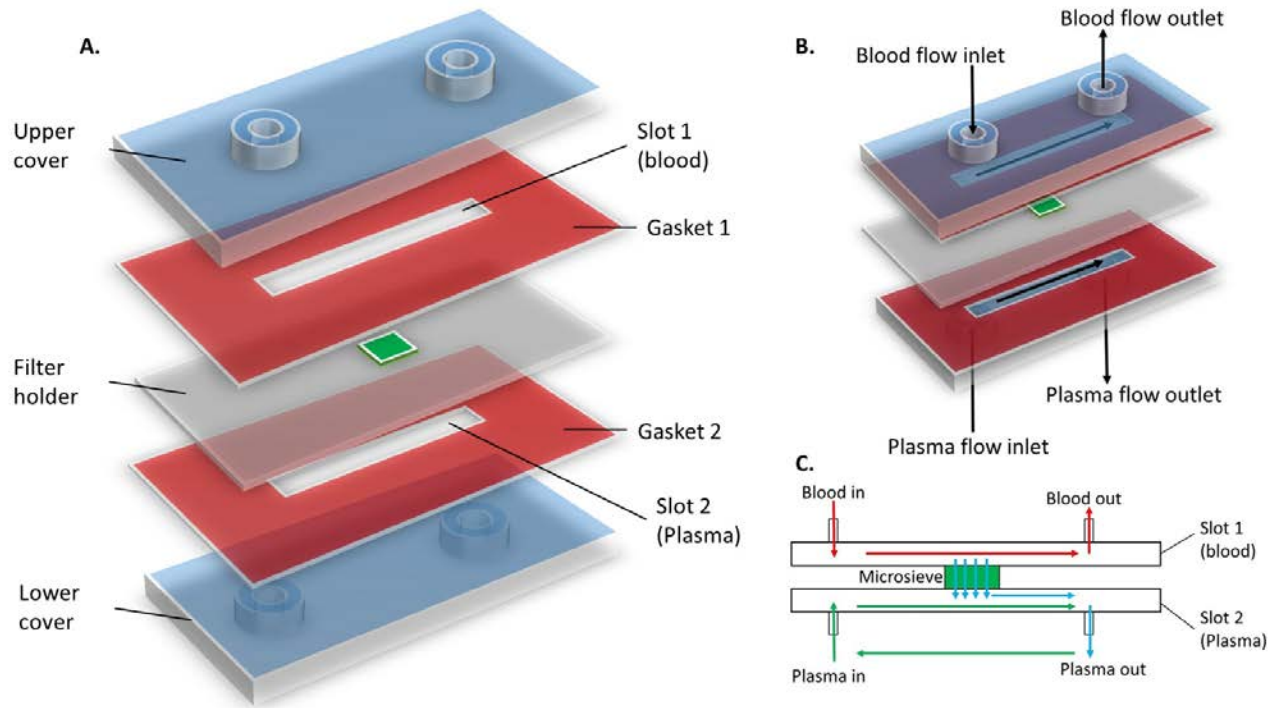


Figure 2. a) Layout of the microfluidic device. b) Semi-assembled device. c) Crossflow schematic – blood/plasma channel layer. Channel dimensions: Length (L) = 3 cm, Width (W)= 9 mm, Blood Height ($2B$)= 200 μm , Plasma Height ($2B$)= 100 μm . The actual channel height was confirmed by water pressure-flow measurements – see Appendix.

The four ports were designated P_1 , P_2 , P_3 , and P_4 . Blood (33% hematocrit) flowed from a reservoir by a peristaltic pump (Bridgemedica, Walpole, MA) into the blood microchannel, through P_1 , and out through P_2 . The plasma flowed through another peristaltic pump (Bridgemedica, Walpole, MA) into the plasma microchannel, through P_3 , and out through P_4 , thus completing a closed loop. Because the peristaltic pump generated pulsatile pressures, pressure dampers (NxStage, Lawrence, MA) were inserted at the points shown in *figure 3*. Filtration was achieved by using a syringe pump (Legato 111 – KD Scientific, Holliston, MA), drawing through a T junction (Small Parts, Inc. Logansport, IN) in the plasma loop. Shear rates

in the device varied from 2000-8000 s^{-1} . To establish the desired operating conditions, blood was drawn at a predetermined flow from an open reservoir by the peristaltic pump (P-1) at a rate which fixes the desired shear rate. For each shear rate, the maximum filtrate flow was measured, at subcritical TMP (the point right before irreversible fouling occurs),¹ by making small increases in the filtrate syringe pump (P-3), thus fixing the maximum flow under the variable TMP (uncompensated) configuration. The filtrate pump was then stopped, and the plasma flow was adjusted by the plasma peristaltic pump (P-2) to establish the cTMP configuration. Once pressures gradients above and below the sieves were equalized (optimal co-current conditions), a new set of maximum filtrate flows were measured for each shear rate by making small increases in the filtrate syringe pump (P-3).

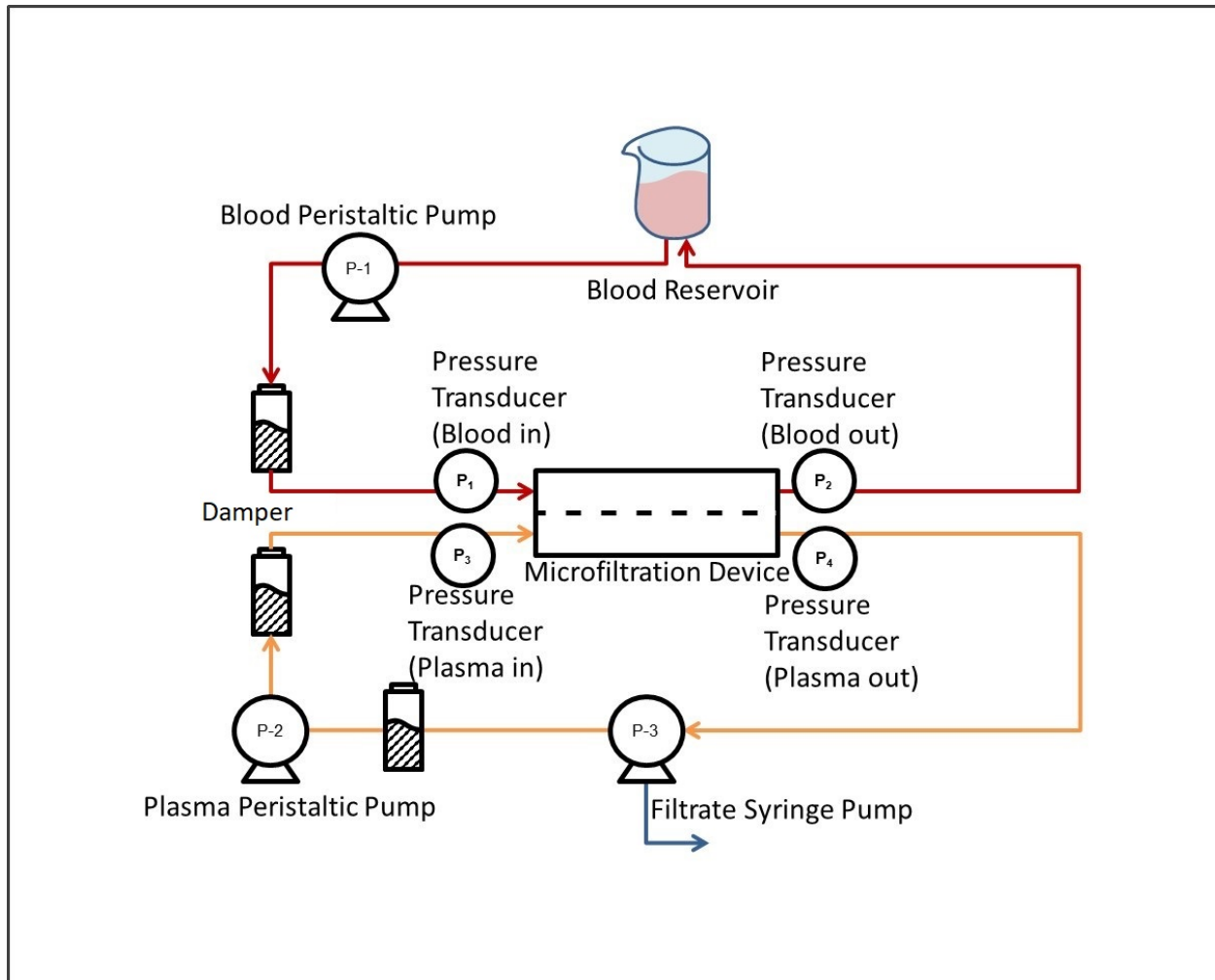


Figure 3. System arrangement including location of the pressure sensors: Blood in (P_1), Blood out (P_2), Plasma in (P_3), and Plasma out (P_4).

2.2 Pressure and Transmembrane Pressure (TMP) Measurements

Four pressure transducers, shown in *figure 3* (Utah Medical Products, Inc), were connected to a data acquisition card (National Instruments cDAQ-9172, TX) to record pressure via a LabView module (National Instruments 9237, TX). The transmembrane pressure (TMP) profile was

computed continuously from the four pressure readings, assuming a linear variation of fluid pressure with axial distance along the channel. The LabView program used *Equation 2.1*:¹⁹

$$TMP = \left(P_1 - \frac{1}{2}(P_1 - P_2) \right) - \left(P_3 - \frac{1}{2}(P_3 - P_4) \right) \quad \text{Equation 2.1}$$

The dimensions shown in *figure 2* were used to estimate the average pressure directly above the filter surface.

2.3 Permeability of Microsieve

Prior to each experiment, the intrinsic permeability of the filter was established by filtering particle-free water through the assembly, as described in detail in the previous study.¹

3. Results & Discussion

3.1 Constant Transmembrane Pressure (cTMP)

Since the feed pressure in a microchannel must decrease along the membrane surface in the direction of flow, the transmembrane pressure against an isobaric filtrate reservoir steadily decreases in the direction of feed flow. If it could remain constant (cTMP), it would allow the entire sieve to work near its critical point, affording larger filtration. This can be achieved by introducing a compensating, decreasing pressure beneath the sieve. Thus, directing filtrate into a channel on the filtrate side of the filter, with a pressure gradient matching that of the feed, can generate cTMP over the entire filtering surface (shown in *Figure 1, column B*). In systems where the feed pressure gradient is constant (because the fraction of the flow that is filtered is small) both gradients are constant. Then, one can expect up to twice the filtration rate obtainable with no pressure variation in the receiving channel, even more if backflow were otherwise allowed to occur, *Figure 1, column A*. cTMP is easily achieved in short channels, but only with more difficulty in longer ones where the overall change in system pressures must equal nearly twice the inlet feed pressure, assuming the channel pressure drop to be much larger than the TMP.

Operating with a cTMP configuration should also lead to greater operational stability with deformable particles (*e.g.* erythrocytes). When erythrocyte suspensions are filtered, sieve performance still increases with transmembrane pressure difference (TMP) but sieves routinely clog if a “critical TMP” is exceeded, as described in detail in the previous study.¹ If this does not occur, the rest of the channel is safe, but the filtering capacity is not fully used. At some risk of clogging, a cTMP configuration allows the entire channel to be operated as close to the critical as one desires.

Results are shown in Table 1. Those under cTMP conditions over a nominal 2 cm filtration length, are compared with those obtained in the absence of a parallel shear flow of the filtrate, as described above. In each case, filtration was slowly increased until clogging was indicated by sharp irreversible increases in TMP. In this manner, maximum filtration rate was determined for each of the 8 conditions studied. Table 1 summarizes these findings:

Shear Rate (s^{-1})	Flux ($cm^3/cm^2\text{-min}$) at sub-critical TMP	
	2000	0.086 ± 0.01
4000	0.177 ± 0.01	0.355 ± 0.01
6000	0.272 ± 0.02	0.505 ± 0.02
8000	0.363 ± 0.02	0.690 ± 0.02
Sieving Configuration	Variable TMP	cTMP

Table 1. Calculated fluxes ($J = Q_f/A_m$) for each sieving configuration. Q_f represents maximum filtration rate at its corresponding shear rate, and A_m corresponds to the sieving area of 2 cm^2 .

At all shear rates, experiments showed the maximum filtrate flux to be nearly twice that obtained without cTMP (Table 1 and figure 4). In principle, the advantage should be exactly twofold, since the filtration rate was insignificant relative to the plasma flow.

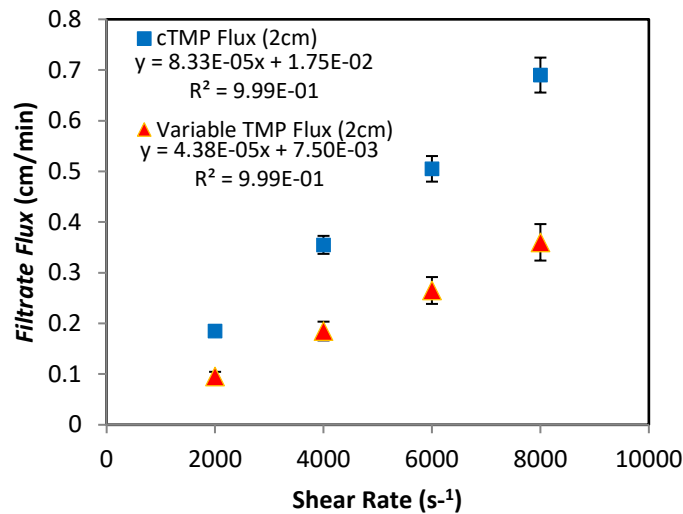


Figure 4. Compares filtration with cTMP (blue squares) to filtration without cTMP (red triangles). The average ratio of the filtrate fluxes through a sieving area of 2 cm² over each set of points is 1.9 ± 0.05 .

If the desired channel is long enough, the effect of a pressure gradient in the filtrate channel can be limited by the inability of the filtrate channel to discharge at a pressure low enough to maintain the inlet TMP over the full filter length. In fact, there can be a point where the pressure at the filtrate side of the sieve becomes higher than the pressure at the permeate side, reversing the TMP and creating a backflow as depicted in *Fig. 1, column A, third row*. This circumstance can be avoided only by raising, equally, all other system pressures.

To test the limits of the cTMP configuration with respect to channel length, the channel described above was increased by joining two $1 \times 2 \text{ cm}^2$ sieves arranged in series to yield a sieving area of $1 \times 4 \text{ cm}^2$. At each shear rate, the filtration rate for the cTMP configuration should still be twice that for the variable TMP configuration. However, when this longer sieving surface

was used, the filtration rate was about 1/3 less than that obtained with cTMP configuration, as depicted in *Table 2*:

Shear Rate (s ⁻¹)	Flux (cm ³ /cm ² -min) at sub-critical TMP	
	Variable TMP	cTMP
2000	0.067 ± 0.01	0.187 ± 0.01
4000	0.127 ± 0.01	0.350 ± 0.01
6000	0.197 ± 0.02	0.520 ± 0.02
8000	0.245 ± 0.02	0.700 ± 0.02
Sieving Configuration	Variable TMP	cTMP

Table 2. Calculated fluxes ($J = Q_f/A_m$) for each sieving configuration, with Q_f representing the maximum filtration rate at its corresponding shear rate, and A_m corresponding to the sieving area of 4 cm².

In other words, under cTMP configuration, the longer (4 cm length) flow path produced the same filtrate flux (flow per unit of filter area) as the original (2 cm length) path (*i.e.* at a shear rate of 8000 s⁻¹, fluxes for 2 and 4 cm² are 0.69 ± 0.02 and 0.70 ± 0.02 cm/min, respectively).

However, the longer path underperformed by about 30% when cTMP was not imposed (*i.e.* at a shear rate of 8000 s⁻¹, fluxes for 2 and 4 cm² are 0.363 ± 0.02 and 0.245 ± 0.02 cm/min, respectively). This “flux loss” may be explained by cumulative blocking, associated from using the same device to get the eight data points at each shear rates for the 2-sieve cell. The deterioration of the sieve (membrane fouling) may have led to the diminishing filtration acquired during the uncompensated modality (variable TMP), specially so as this non cTMP configurations are less protected by sudden operational instability (*e.g.* pressure surges).

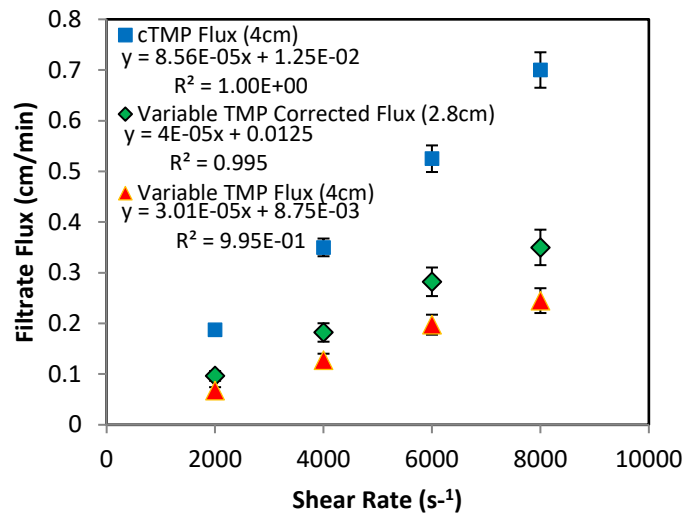


Figure 5. Compares filtration with cTMP (blue squares) to filtration without cTMP (red triangles). In theory (green diamonds), the cTMP advantage should be exactly twofold, given that the filtration rate is insignificant relative to the plasma flow. However, fluxes under variable TMP configuration significantly diminish when a longer flow path (4 cm²) was studied. Most probably due to cumulative accumulation membrane fouling from multiple runs.

Filtration longevity was also benefitted by the cTMP configuration. Accordingly, experiments have shown that the TMP profile remains stable for 5 hours at fluxes of about 0.7 cm³/cm²-min (Table 1 and Table 2), with elective termination. We believe under cTMP configuration, scaling up may be achieved to extract medically relevant amounts of plasma from blood, safely and in real time. There may also be benefits to other industrial applications.

4. Conclusion

In microfluidic blood filtration, sieve performance increases with transmembrane pressure difference (TMP), but sieves routinely clog if a “critical” transmembrane pressure difference is exceeded. In a microfluidic channel, TMP decreases in the direction of suspension flow; and if the system is calibrated to avoid clogging at the inlet, a linear drop to zero TMP at the outlet causes the channel to operate at only half of its potential capacity. Setting a safe TMP at the leading edge of the sieve, minimizes the possibility of its clogging there; while imposing a constant TMP over the whole surface, as defined in this paper, maintains the entrance flux everywhere.

A constant TMP (cTMP) regimen, that results in a constant trans-sieve pressure difference along the length of the sieve, allows near doubling of filtrate flux over the entire sieve area at a flux with a TMP comfortably below the critical value.

5. Acknowledgements

Support for this work was provided in part by Grant 1R21HL088162 from the National Institute of Health, and Vizio Medical Devices, LLC. The authors also thank Columbia Medical Center Blood Bank and blood donors. We acknowledge gratefully the assistance of Dr. Robert von Gutfeld as well as our whole medical team, most especially the late Dr. James Jones.

6. Appendix

6.1 Nomenclature

B	Half height of the channel (m)
L	Channel Length (m)
W	Channel width (m)
ΔP	Pressure drop across the channel (Torr)
Q_f	Volumetric flowrate of the permeate (<i>i.e.</i> Filtration rate) (cm ³ /min)
Q_m	Volumetric flowrate in main channel (cm ³ /min)
TMP	Transmembrane pressure (Torr)
J_f	Filtrate flux (cm ³ /cm ² -min)
P_1	Inlet blood pressure (Torr)
P_2	Outlet blood pressure (Torr)
P_3	Inlet plasma pressure (Torr)
P_4	Outlet plasma pressure (Torr)

Greek symbols

γ_w	Nominal wall shear rate (1/s)
τ_w	Wall shear stress (Pa)
μ	Viscosity of media (Poise)

6.2 Supporting Equations:

Microchannel Height

As in a previous study,¹ the thickness of each microchannel varied each time the apparatus was assembled and had to be accurately calculated each time. By measuring the change in pressure for various through-flow rates for a fluid of known viscosity (*i.e.* microfiltered water), the thickness ($2B$) of the channel was calculated using the equation for laminar flow in a narrow slit solved for B :¹⁹

$$2B = 2 \times \sqrt[3]{\frac{3 \mu L}{2 W} \times \frac{Q_m}{\Delta P}} \quad \text{Equation 6.1}$$

The flow was assumed to be Newtonian, laminar, and fully developed, where Q_m is the volumetric flow rate, ΔP is the difference in pressure between inlet and outlet, W and L are the width and length of the channel, respectively, and μ is the viscosity of the fluid.¹⁹

Since the heights above and below the microsieves were not equal, different flows above and below the sieves were required to create the same pressure drop. A simplified version of the slit flow equation¹⁹ was used:

$$Q_{plasma} = \left(\frac{3}{2}\right) Q_{blood} \left(\frac{B_{plasma}}{B_{blood}}\right)^3 \quad \text{Equation 6.2}$$

The factor $3/2$ compensates for the viscosity difference between the two fluids.

Shear Rate and Shear Stress at the Wall

The shear stress exerted at the flow boundaries, τ_w can be calculated by balancing the shear force at the wall against the pressure gradient for a slit channel.¹⁹

$$\tau_w = \frac{\mu 3 Q_m}{2 B^2 W} \quad \text{Equation 6.3}$$

Shear rates ($\dot{\gamma} = \frac{dV}{dz}$) at the wall are found as the shear stress (τ_w) divided by the viscosity:

$$\gamma_w = \frac{\tau_w}{\mu} = \frac{3Q_m}{2B^2W} \quad \text{Equation 6.4}$$

where Q_m is the volumetric flow rate, B is the half thickness of the channel, W is the width of the channel, and μ is the viscosity of the fluid.¹⁹

7. References

1. Amar LI, Guisado D, Faria M, et al. Erythrocyte fouling on micro-engineered membranes. *Biomedical microdevices* 2018;20:55.
2. Dickson M, Amar L, Hill M, Schwartz J, Leonard E. A scalable, micropore, platelet rich plasma separation device. *Biomed Microdevices* 2012;14:1095-102.
3. Charcosset C. Membrane processes in biotechnology: an overview. *Biotechnology advances* 2006;24:482-92.
4. Rossignol N, Vandanjon L, Jaouen P, Quemeneur F. Membrane technology for the continuous separation microalgae/culture medium: compared performances of cross-flow microfiltration and ultrafiltration. *Aquacultural Engineering* 1999;20:191-208.
5. Maria MS, Kumar B, Chandra T, Sen A. Development of a microfluidic device for cell concentration and blood cell-plasma separation. *Biomedical microdevices* 2015;17:115.
6. Rodrigues RO, Pinho D, Faustino V, Lima R. A simple microfluidic device for the deformability assessment of blood cells in a continuous flow. *Biomedical microdevices* 2015;17:108.
7. van Rijn CJ, Nijdam W, Kuiper S, Veldhuis GJ, van Wolferen H, Elwenspoek M. Microsieves made with laser interference lithography for micro-filtration applications. *Journal of Micromechanics and Microengineering* 1999;9:170.
8. Ji HM, Samper V, Chen Y, Heng CK, Lim TM, Yobas L. Silicon-based microfilters for whole blood cell separation. *Biomedical microdevices* 2008;10:251-7.
9. Dickson MN, Amar L, Hill M, Schwartz J, Leonard EF. A scalable, micropore, platelet rich plasma separation device. *Biomedical microdevices* 2012;14:1095-102.
10. Weeranoppanant N, Amar L, Tong E, Faria M, Hill MI, Leonard EF. Modeling of Fouling in Cross-flow Microfiltration of Suspensions. *AIChE Journal* 2018.
11. Drew DA, Schonberg JA, Belfort G. Lateral inertial migration of a small sphere in fast laminar flow through a membrane duct. *Chemical engineering science* 1991;46:3219-24.
12. Zydney AL, Colton CK. A Concentration Polarization Model For The Filtrate Flux In Cross-Flow Microfiltration Of Particulate Suspensions. *Chemical Engineering Communications* 1986;47:1-21.
13. Mackley MR, Sherman NE. Cross-flow cake filtration mechanisms and kinetics. *Chemical Engineering Science* 1992;47:3067-84.

14. Kromkamp J, Bastiaanse A, Swarts J, Brans G, van der Sman RGM, Boom RM. A Suspension Flow Model For Hydrodynamics And Concentration Polarisation In Crossflow Microfiltration. *Journal of Membrane Science* 2005;253:67-79.
15. Leonard EF, Vassilieff CS. The Deposition Of Rejected Matter In Membrane Separation Processes. *Chemical Engineering Communications* 1984;30:209-17.
16. Field RW, Wu D, Howell JA, Gupta BB. Critical flux concept for microfiltration fouling. *Journal of membrane science* 1995;100:259-72.
17. Wagdare NA, Marcelis AT, Ho OB, Boom RM, van Rijn CJ. High throughput vegetable oil-in-water emulsification with a high porosity micro-engineered membrane. *Journal of Membrane Science* 2010;347:1-7.
18. van Rijn CJ. *Nano and micro engineered membrane technology*: Elsevier; 2004.
19. Bird RB, Stewart WE, Lightfoot EN. *Transport Phenomena*: Wiley; 2007.

Chapter 5

Conclusion

In this thesis, we have analyzed crossflow microfiltration of different suspensions, with special interest in the practical removal of plasma from suspended erythrocytes by filtration, using a thin silicon nitride layer photolithographically patterned with micron-sized pores. In all studies, we have concluded that the filtrate flux is directly proportional to the transmembrane pressure (TMP) and surface shear rate, in agreement with classical concentration polarization theory.

The effect of the high deformability of erythrocytes was analyzed and is addressed in Chapter 2 (*Figure 6*). At steady state, a significant increase in resistance to filtration was seen for all media studied regardless of pore size and shape (Section 3.2). We attribute this resistance to a non-negligible, stationary monolayer of erythrocytes which forms on the filter surface anchoring themselves by extension into the pores during filtration (Section 3.1, *Figure 5*). It appears that with the formation of this monolayer, the filtration resistance becomes primarily dependent on the anchored layer of retentate (erythrocytes) which, however, is seen to be incomplete (*Figures 7 and 8*). This buildup of particles seems to be a direct consequence of erythrocyte capture and not upon any conventional fouling mechanism (*Figure 3.2.2*).

Contrary to classical theory, the inflowing erythrocyte concentration (hematocrit) does not affect steady state permeation rates; it affects only their rate of approach to steady state (*Figure 8*). This incomplete layer appears to prevent further cell adherence to the sieving surface (Section 3.1).

High shear flows thus appear to prevent formation of multilayers, allowing steady state filtration to be achieved (Section 3.1).

In Chapter 3, cross-flow (tangential) microfiltration of a suspension of uniform beads was modeled and interpreted as a force balance at the interface between a stationary filter cake and a feed stream moving over it. For a suspension - composed of uniform, hard spherical beads - a

first-principles model was built and was successfully compared with experimental data. Other systems (*i.e.* erythrocytes) may present a more complex interfacial geometry and pore structure. However, such systems should preserve the fundamental findings of this research: that interfacial mechanics, and not particle migration, determine the fraction of a microfilter's cross-section that is available for through-flow.

The essence of this model is that in the crowded space of a microfluidic filter, the feed flows through a narrow slit, sharing the slit height with a stationary filter cake. Thus, a self-sustaining force balance is achieved. This force balance sets and maintains a split in slit height. By measuring TMP for various filtrate and main flowrates, the minimum flowrate and critical shear stress to prevent unstable packed bed formation were found and related to the main flowrate, filtrate flowrate, and particle size. A linear relationship was found between critical wall shear stress and filtrate flowrate, an inverse relationship between particle size and critical wall shear stress, but with no relationship between the main flowrate and the critical wall shear stress, all in support of the proposed model.

One cannot expect such clear and simple relationships for particles that are more complex in shape and size. However, the underlying phenomenology is likely to be preserved providing a basis for understanding and correlating observations in such systems. Further work will be needed to analyze less uniform particle beds as the deformation provided by erythrocytes.

Chapter 4 addresses a more fundamental generic problem regarding filtration. In systems where trans-membrane pressure is allowed to change strongly with axial position, a 'marching' increase in filter resistance with time was seen and attributed to slow augmentation of cellular adhesion growing from the blood inlet. Since pressure in a microchannel must decrease in the direction of

flow, and pressure on the permeate side of a crossflow membrane is uniform, the TMP must decrease in the direction of suspension flow. This limits the maximum TMP to that experienced along the membrane occurring at its leading edge. If the TMP at the leading edge is sufficiently high, erythrocytes will be irreversibly squeezed into the membrane pores, causing a fouling stagnant layer of erythrocytes in this region. If filtration rate remains unchanged, TMP will increase leading to more of the membrane seeing a sufficiently high TMP so as to cause an erythrocyte fouling cascade, and hence the fouled region will propagate along the membrane until the entire membrane is fouled.

By introducing a carefully designed flow channel on the permeate side beneath the membrane, we were able to permit the pressure on the permeate side of the membrane to decrease along the length of the membrane, and thereby achieve a constant TMP along the complete membrane. This allowed for the entire membrane to be used at a pressure below that leading to erythrocyte fouling, permitting a higher stable filtration rate than reported in chapter 2.

As a result, a constant TMP (cTMP) regimen, that results in a constant trans-sieve pressure difference along the length of the sieve, allows near doubling of filtrate flux over the entire sieve area at a flux with a TMP comfortably below the critical value. Further work will be needed to analyze this modality with other suspensions. However, the underlying phenomenon is likely to be preserved and to provide a higher throughput and stable filtration environment than conventional crossflow microfiltration.